ATLAS CONF Note

ATLAS-CONF-2017-071

18th September 2017

Measurement of the top quark mass in the $t\bar{t} \rightarrow$ lepton+jets channel from $\sqrt{s} = 8$ TeV ATLAS data

The ATLAS Collaboration

The top quark mass is measured using a template method in the $t\bar{t} \rightarrow$ lepton + jets channel (lepton = e, μ) using ATLAS data recorded in the year 2012 at the LHC. The data were taken at a proton–proton centre-of-mass energy of $\sqrt{s} = 8$ TeV and correspond to an integrated luminosity of 20.2 fb^{-1}. The $t\bar{t} \rightarrow$ lepton + jets channel is characterised by the presence of a charged lepton, a neutrino and at least four jets, two of which originate from bottom quarks (b-jets). Exploiting a three-dimensional template technique, the top-quark mass is determined together with a global jet energy scale factor and a relative b-to-light-jet energy scale factor. The mass of the top quark is measured to be $m_{\text{top}} = 172.08 \pm 0.39\,(\text{stat}) \pm 0.82\,(\text{syst})$ GeV, with a total uncertainty of 0.91 GeV. A combination with previous ATLAS m_{top} measurements is performed and results in $m_{\text{top}} = 172.51 \pm 0.27\,(\text{stat}) \pm 0.42\,(\text{syst})$ GeV, with a total uncertainty of 0.50 GeV.

ATLAS-CONF-2017-071
25 September 2017

1 Introduction

The mass of the top quark (m_{top}) is an important parameter of the Standard Model (SM). Precise measurements of m_{top} provide crucial information for global fits of electroweak parameters [1–3] which help to assess the internal consistency of the SM and to probe its extensions. In addition, the value of m_{top} affects the stability of the SM Higgs potential, which has cosmological implications [4–6].

Many measurements of m_{top} in each $t\bar{t}$ decay channel have been performed by the Tevatron and LHC collaborations. The most precise measurements per experiment in the $t\bar{t} \to$ lepton + jets channel are: $m_{\text{top}} = 172.85 \pm 0.71\,(\text{stat}) \pm 0.84\,(\text{syst})$ GeV by CDF [7][1], $m_{\text{top}} = 174.98 \pm 0.58\,(\text{stat}) \pm 0.49\,(\text{syst})$ GeV by D0 [8], $m_{\text{top}} = 172.33 \pm 0.75\,(\text{stat}) \pm 1.03\,(\text{syst})$ GeV by ATLAS [9] and $m_{\text{top}} = 172.35 \pm 0.16\,(\text{stat}) \pm 0.48\,(\text{syst})$ GeV by CMS [10]. Combinations are performed, by either the individual experiments, or by several Tevatron and LHC experiments [11]. In these combinations selections of measurements from all $t\bar{t}$ decay channels are used. The latest combinations per experiment are: $m_{\text{top}} = 173.16 \pm 0.57\,(\text{stat}) \pm 0.74\,(\text{syst})$ GeV by CDF [12], $m_{\text{top}} = 174.95 \pm 0.40\,(\text{stat}) \pm 0.64\,(\text{syst})$ GeV by D0 [13], $m_{\text{top}} = 172.84 \pm 0.34\,(\text{stat}) \pm 0.61\,(\text{syst})$ GeV by ATLAS [14] and $m_{\text{top}} = 172.44 \pm 0.13\,(\text{stat}) \pm 0.47\,(\text{syst})$ GeV by CMS [10].

In this paper a new ATLAS measurement of m_{top}, obtained in the $t\bar{t} \to$ lepton + jets channel, is presented. The analysis exploits the decay $t\bar{t} \to W^+W^-b\bar{b} \to \ell\nu q\bar{q}'b\bar{b}$, which is realised when one W boson decays into a charged lepton ($\ell = e, \mu$ including $\tau \to e, \mu$ decays) and a neutrino (ν), and the other into a pair of quarks. In the analysis presented here, the electron+jets and muon+jets final states are combined and referred to as the $t\bar{t} \to$ lepton + jets channel. Single-top-quark events with the same reconstructed final states contain information about the top quark mass and are therefore taken into account as signal events.

The measurement is based on a template method. In this method, simulated distributions are constructed for a chosen quantity sensitive to the physics parameter under study, using a number of discrete values of that parameter. These templates are fitted to functions that interpolate between different input values of the physics parameter, fixing all other parameters of the functions. In the final step, an unbinned likelihood fit to the observed data distribution is used to obtain the value of the physics parameter that best describes the data. In this procedure, the experimental distributions are constructed such that they are unbiased estimators of the physics parameter used as input in the signal Monte Carlo (MC) samples. Consequently, the top quark mass determined in this way corresponds to the mass definition used in the MC simulation. Because of various steps in the MC event simulation, the mass measured this way does not directly coincide with mass definitions within a given renormalisation scheme, e.g. the top quark pole mass. Evaluating the differences is a topic of theoretical investigations [15–17].

The measurement exploits the three-dimensional template fit technique presented in Ref. [9]. To reduce the uncertainty in m_{top} stemming from the uncertainties in the jet energy scale (JES) and the additional b-jet energy scale (bJES), m_{top} is measured together with the jet energy scale factor (JSF) and the relative b-to-light-jet energy scale factor (bJSF). Given the larger data sample compared to Ref. [9], the analysis presented here is optimised to reject combinatorial background, i.e. events with wrongly assigned jets, thereby achieving a smaller total uncertainty. Given this new measurement, an update of the ATLAS combination of m_{top} measurements is also presented.

[1] Natural units are used throughout this note, i.e. $c = \hbar = 1$. Consequently, masses, momenta and energies carry the same unit, GeV.

This document is organised as follows: after a short description of the ATLAS detector in Section 2, the data and MC simulation samples are discussed in Section 3. Details of the event selection are given in Section 4. The optimisation of the event selection using a multivariate analysis approach is presented in Section 5. The template fits are introduced in Section 6. The evaluation of the systematic uncertainties and their statistical uncertainties are discussed in Section 7 and the measurement of m_{top} is given in Section 8. The combination of this measurement with previous ATLAS measurements is discussed in Section 9 and compared to measurements of other experiments. Finally, the summary and conclusions are given in Section 10.

2 The ATLAS experiment

The ATLAS experiment [18] at the LHC is a multi-purpose particle detector with a forward-backward symmetric cylindrical geometry and a near 4π coverage in the solid angle.[2] It consists of an inner tracking detector surrounded by a thin superconducting solenoid providing a 2 T axial magnetic field, electromagnetic and hadronic calorimeters, and a muon spectrometer. The inner tracking detector covers the pseudorapidity range $|\eta| < 2.5$. It consists of silicon pixel, silicon micro-strip, and transition radiation tracking detectors. Lead/liquid-argon (LAr) sampling calorimeters provide electromagnetic (EM) energy measurements with high granularity. A hadronic (steel/scintillator-tile) calorimeter covers the central pseudorapidity range ($|\eta| < 1.7$). The end-cap and forward regions are instrumented with LAr calorimeters for both EM and hadronic energy measurements up to $|\eta| = 4.9$. The muon spectrometer surrounds the calorimeters and is based on three large air-core toroid superconducting magnets with eight coils each. Its bending power is in the range from 2.0 to 7.5 T m. It includes a system of precision tracking chambers and fast detectors for triggering. A three-level trigger system is used to select events. The first-level trigger is implemented in hardware and uses a subset of the detector information to reduce the accepted rate to at most 75 kHz. This is followed by two software-based trigger levels that together reduce the accepted event rate to 400 Hz on average depending on the data-taking conditions during 2012.

3 Data and MC samples

The analysis is based on pp collision data recorded by the ATLAS detector in 2012 at a centre-of-mass energy of $\sqrt{s} = 8$ TeV. The integrated luminosity amounts to 20.2 fb^{-1}with an uncertainty of 1.9% [19]. This was measured using data from dedicated van-der-Meer scans. The modelling of top quark pair ($t\bar{t}$) and single-top-quark signal events, as well as most background processes, relies on MC simulations. For the simulation of $t\bar{t}$ signal events the Powheg-Box v2 [20–22] generator is used, while the Powheg-Box v1 generator is used for the simulation of single-top-quark events. Within this framework, the simulations of the top quark pair [23] and single-top-quark production in the s- and t-channel [24], and the Wt-channel [25] use matrix elements at next-to-leading order (NLO) in the strong coupling constant α_{S},

[2] ATLAS uses a right-handed coordinate system with its origin at the nominal interaction point (IP) in the centre of the detector and the z-axis along the beam pipe. The x-axis points from the IP to the centre of the LHC ring, and the y-axis points upwards. Cylindrical coordinates (r, ϕ) are used in the transverse plane, ϕ being the azimuthal angle around the z-axis. The pseudorapidity is defined in terms of the polar angle θ as $\eta = -\ln\tan(\theta/2)$. Angular distance is measured in units of $\Delta R \equiv \sqrt{(\Delta\eta)^2 + (\Delta\phi)^2}$.

with the NLO CT10 [26] parton distribution function (PDF) set and the parameter $h_{\text{damp}} = \infty$.[3] Taking into account the top quark mass m_{top} and transverse momentum p_{T} for the underlying Born configuration (i.e. before radiation), the dynamic factorisation and renormalisation scales were set to $\sqrt{m_{\text{top}}^2 + p_{\text{T}}^2}$. The Pythia (v6.425) program [27] with the P2011C [28] set of tunable parameters (tune) and the corresponding CTEQ6L1 PDFs [29] are employed to provide the parton shower (PS), hadronisation and underlying-event modelling.

For m_{top} hypothesis testing, the $t\bar{t}$ and single-top-quark event samples are generated for five different assumed values of m_{top} in the range 167.5 to 177.5 GeV in steps of 2.5 GeV. For each m_{top} value, the MC samples are normalised according to the best available cross-section calculations. For $m_{\text{top}} = 172.5$ GeV, the $t\bar{t}$ cross-section amounts to $\sigma_{t\bar{t}} = 253^{+13}_{-15}$ pb, calculated at next-to-next-to-leading order (NNLO) with next-to-next-to-leading logarithmic soft gluon terms [30–34] with the Top++ 2.0 program [35]. The cross-sections for single-top-quark production are calculated at NLO and amount to $\sigma_{\text{t}} = 87.8^{+3.4}_{-1.9}$ pb [36], $\sigma_{Wt} = 22.4 \pm 1.5$ pb [37] and $\sigma_{\text{s}} = 5.6 \pm 0.2$ pb [38] in the t-, the Wt- and the s-channel, respectively. The PDF and α_{S} uncertainties in these cross-sections are calculated using the PDF4LHC prescription [39] with the MSTW2008 68% CL NNLO PDF [40, 41], CT10 NNLO PDF [26, 42] and NNPDF2.3 5f FFN PDF [43], and are added in quadrature with the uncertainties obtained from the variation of the factorisation and renormalisation scales by factors of 0.5 and 2.0.

The Alpgen (v2.13) program [44] interfaced to the Pythia6 program is used for the simulation of $W^{\pm}$ or Z bosons in association with jets. The CTEQ6L1 PDFs and the corresponding AUET2 tune [45] are used for the matrix element and PS settings. The W+jets and Z+jets events containing heavy-flavour (HF) quarks (W/Zbb+jets, W/Zcc+jets, and Wc+jets) are generated separately using matrix elements at leading order (LO) involving massive bottom and charm quarks. Double-counting of HF quarks in the matrix element and the PS evolution is avoided via a HF overlap-removal procedure that uses the ΔR between the additional heavy quarks as criterion. If the ΔR is smaller than 0.4, the parton shower prediction is taken. For larger values, the matrix element prediction is used. The W+jets and Z+jets samples are normalised to the inclusive NNLO calculation [46]. Due to the large uncertainties on the overall W+jets normalisation and the flavour composition, both are estimated using data-driven techniques as described in Section 4.2. Diboson production processes (WW, WZ and ZZ) are simulated using the Alpgen program with CTEQ6L1 PDFs. They are interfaced to the Herwig (v6.520) [47] and Jimmy (v4.31) [48] programs. The samples are normalised to their predicted values at NLO [49].

All samples are simulated taking into account the effects of multiple soft pp interactions (pile-up) that are present in the 2012 data. These interactions are modelled by overlaying simulated hits from events with exactly one inelastic collision per bunch crossing with hits from minimum-bias events that are produced with the Pythia (v8.160) program [50] using the A2M tune [51] and the MSTW2008 LO PDF.

The samples undergo a simulation of the ATLAS detector [52] based on Geant4 [53] and are then processed through the same reconstruction software as the data. A number of samples used to assess systematic uncertainties are produced bypassing the highly computing-intensive full Geant4 simulation. They are produced with a faster version of the simulation [54], which retains the full simulation of the tracking. However, to approximate the results of the full simulation, it uses a parameterised calorimeter response, based on resolution functions measured in full simulation samples.

[3] The h_{damp} parameter controls the transverse momentum p_{T} of the first additional emission beyond the Born configuration in the parton shower and therefore regulates the high-p_{T} emission against which the $t\bar{t}$ system recoils.

4 Object reconstruction, background estimation and event preselection

The detector objects resulting from the top quark pair decay are electron and muon candidates, jets and missing transverse momentum ($E_{\mathrm{T}}^{\mathrm{miss}}$). In the MC simulation events, corrections are applied to all these objects based on detailed data-to-MC comparisons for many different processes, so as to match their performance in data.

4.1 Object reconstruction

Electron candidates [55] are required to have a transverse energy of $E_{\mathrm{T}} > 25$ GeV, a pseudorapidity of the corresponding EM cluster of $|\eta_{\mathrm{cluster}}| < 2.47$, with the transition region $1.37 < |\eta_{\mathrm{cluster}}| < 1.52$ between the barrel and the end-cap calorimeter excluded. Muon candidates [56] are required to have transverse momentum $p_{\mathrm{T}} > 25$ GeV and $|\eta| < 2.5$. To reduce the contamination by leptons from HF decays inside jets or from photon conversions, referred to as non-prompt (NP) leptons, strict isolation criteria are applied to the amount of activity in the vicinity of the lepton candidate [55–57].

Jets are built from topological clusters of calorimeter cells [58] with the anti-k_t jet clustering algorithm [59], using a radius parameter of $R = 0.4$. The clusters are calibrated using the local cluster weighting (LCW) and global sequential calibration (GSC) algorithm [60–62]. The subtraction of the contributions from pile-up is performed via the jet area method. This procedure is based on the observation that pile-up is a uniform and diffuse background, which adds momentum to each jet [63]. In this method, the per event average p_{T} density in the η-ϕ plane is determined and subtracted, based on a definition of the jet area that uses equally distributed artificial particles with negligible p_{T} in the jet clustering. Jets are calibrated using an energy- and η-dependent simulation-based scheme, with in-situ corrections based on data [61]. Jets originating from pile-up interactions are identified via their jet vertex fraction (JVF), the p_{T} fraction of associated tracks stemming from the primary vertex. The requirement $|\mathrm{JVF}| > 0.5$ is solely applied to jets with $p_{\mathrm{T}} < 50$ GeV and $|\eta| < 2.4$. Jets outside of this phase space are always accepted [63]. Finally, jets are required to satisfy $p_{\mathrm{T}} > 25$ GeV and $|\eta| < 2.5$.

Muons reconstructed within a $\Delta R = 0.4$ cone around the axis of a jet with $p_{\mathrm{T}} > 25$ GeV are not considered as lepton candidates. In addition, the closest jet within a $\Delta R = 0.2$ cone around an electron candidate is removed, and finally electrons within a $\Delta R = 0.4$ cone around any of the remaining jets are discarded.

The identification of jets containing b-hadrons, called b-tagging, is used for event reconstruction and background suppression. In the following, irrespective of their origin, jets tagged by the b-tagging algorithm are referred to as b-tagged jets, whereas those not tagged are referred to as untagged jets. Similarly, whether they are tagged or not, jets originating from bottom quarks are referred to as b-jets and those from (u, d, c, s)-quarks or gluons as light jets. The working point of the neural-network-based MV1 b-tagging algorithm [64] corresponds to an average b-tagging efficiency of 70% for b-jets in simulated $t\bar{t}$ events and rejection factors of 5 for jets containing a c-hadron and 140 for jets containing only lighter-flavour hadrons. To match the b-tagging performance in the data, p_{T}- and η-dependent scale factors [64], obtained from dijet and $t\bar{t} \rightarrow$ dilepton events, are applied to MC jets depending on their true flavour.

The missing transverse momentum $E_{\mathrm{T}}^{\mathrm{miss}}$ is the absolute value of the vector ($\overrightarrow{E_{\mathrm{T}}}^{\mathrm{miss}}$) calculated from the negative vectorial sum of all transverse momenta. The vectorial sum takes into account all energy deposits in the calorimeters, projected onto the transverse plane. The clusters are corrected using the calibrations

that belong to the associated physics object. Muons are included in the calculation of the $E_{\mathrm{T}}^{\mathrm{miss}}$ using their reconstructed momentum in the tracking detectors [65].

4.2 Background estimation

The contribution of events wrongly reconstructed as $t\bar{t} \to$ lepton + jets events due to the presence of objects misidentified as leptons (fake leptons) and NP leptons originating from HF decays, is estimated from data using the matrix-method [66]. The technique employed uses fake-lepton and real-lepton efficiencies that depend on η and p_{T}, measured in a background-enhanced control region with low $E_{\mathrm{T}}^{\mathrm{miss}}$ and from events with dilepton masses around the Z peak [67]. For the W+jets background, the overall normalisation is estimated from data. The estimate is based on the charge-asymmetry method [68], relying on the fact that at the LHC more W^+ bosons than W^- bosons are produced. In addition, a data-driven estimate of the $Wb\bar{b}/Wc\bar{c}$, the Wc and the W+light-jet fractions is performed in events with exactly two jets and at least one b-tagged jet. Further details are given in Ref. [69]. The Z+jets and diboson background processes are normalised to their predicted cross-sections in MC as described in Section 3.

4.3 Event preselection

Triggering of events is solely based on the presence of a single electron or muon and no information from the hadronic final state is used. A logical *OR* of two triggers is used for each of the $t\bar{t} \to$ electron + jets and $t\bar{t} \to$ muon + jets channels. The triggers with the lower thresholds of 24 GeV for electrons or muons select isolated leptons. The triggers with the higher thresholds of 60 GeV for electrons and 36 GeV for muons do not include an isolation requirement. The selection requirements follow closely those in Ref. [9] and are listed below:

1. Events are required to have at least one primary vertex with at least five associated tracks. The tracks need to have a minimum p_{T} of 400 MeV. For events with more than one primary vertex, the one with the largest $\sum p_{\mathrm{T}}^2$ is chosen as the vertex from the hard scattering.
2. The event must contain exactly one reconstructed charged lepton with $E_{\mathrm{T}} > 25$ GeV for electrons and $p_{\mathrm{T}} > 25$ GeV for muons that also matches the corresponding trigger object.
3. In the $t\bar{t} \to$ muon + jets channel, $E_{\mathrm{T}}^{\mathrm{miss}} > 20$ GeV and $E_{\mathrm{T}}^{\mathrm{miss}} + m_{\mathrm{T}}^{W} > 60$ GeV are required.[4]
4. In the $t\bar{t} \to$ electron + jets channel, more stringent requirements on $E_{\mathrm{T}}^{\mathrm{miss}}$ and m_{T}^{W} are applied because of the higher level of NP/fake-lepton background. The requirements are: $E_{\mathrm{T}}^{\mathrm{miss}} > 30$ GeV and $m_{\mathrm{T}}^{W} > 30$ GeV.
5. The presence of at least four jets with $p_{\mathrm{T}} > 25$ GeV and $|\eta| < 2.5$ is required.
6. The presence of exactly two b-tagged jets is required.

[4] Here m_{T}^{W} is the W boson transverse mass, defined as $\sqrt{2\, p_{\mathrm{T}}^{\ell}\, E_{\mathrm{T}}^{\mathrm{miss}} \left(1 - \cos\phi(\ell, \overrightarrow{E_{\mathrm{T}}}^{\mathrm{miss}})\right)}$, where $\overrightarrow{E_{\mathrm{T}}}^{\mathrm{miss}}$ provides the neutrino information.

Selection	Preselection		BDT selection	
Data	96105		38054	
$t\bar{t}$ signal	85000 ±	10000	36100 ±	5500
Single-top-quark signal	4220 ±	360	883 ±	85
NP/fake leptons (data-driven)	700 ±	700	9.2 ±	9.2
W+jets (data-driven)	2800 ±	700	300 ±	100
Z+jets	430 ±	230	58 ±	33
$WW/WZ/ZZ$	63 ±	32	7.0 ±	5.2
Signal+background	93000 ±	10000	37300 ±	5500
Expected background fraction	0.043 ±	0.012	0.010 ±	0.003
Data / (Signal+background)	1.03 ±	0.12	1.02 ±	0.15

Table 1: The observed numbers of events in data after the event preselection and the BDT selection (see Section 5). In addition, the expected numbers of signal events for $m_{\text{top}} = 172.5$ GeV and background events corresponding to the integrated data luminosity are given. The uncertainties of the predicted number of events take into account the statistical and systematic sources explained in the text.

This selection is orthogonal to the selection used for the measurement of m_{top} in the $t\bar{t} \rightarrow$ dilepton channel at 8 TeV [14]. The observed number of events in the data after this preselection, together with the expected numbers of signal and background events corresponding to the integrated data luminosity, are given in Table 1. For all predictions, the uncertainties are estimated as the sum in quadrature of the statistical uncertainty, the uncertainty in the integrated luminosity, and all systematic uncertainties assigned to the measurement of m_{top} listed in Section 7, except for the *PDF* and *Pile-up* induced uncertainties which are small. The normalisation uncertainties listed below are included for the predictions shown in this section, but due to their small impact on the top quark mass they are not included in the final measurement.

For the signal, the 5.7% uncertainty in the $t\bar{t}$ cross-section as introduced in Section 3, and a 6.0% uncertainty in the single-top-quark cross-section are used. The latter uncertainty is obtained from the cross-section uncertainties given in Section 3 and the relative rates of the various single-top-quark contributions after the selection requirements. The background uncertainties contain uncertainties of 48% in the normalisation of the diboson production processes. They are calculated using Berends-Giele-scaling [70], as done for the Z+jets uncertainty. Assuming a top quark mass of $m_{\text{top}} = 172.5$ GeV, the predicted number of events is consistent with the one observed in the data within uncertainties.

Given the good description of the observed number of events by the prediction, and that the measurement of m_{top} is mostly sensitive to the shape of the distributions, the comparison of the data to the predictions is solely based on distributions normalised to the number of events observed in data. The systematic uncertainty assigned to each bin is calculated from the quadratic sum of all systematic uncertainties discussed above.

Some distributions of the observed event kinematics for the event preselection are shown in Figure 1. The observed distributions agree with the predictions within uncertainties. This applies to the observed transverse momentum of the leptons, shown in Figure 1(a), the average transverse momentum of the jets, shown in Figure 1(b), the transverse momentum of the hadronically decaying top quark ($p_{\text{T,had}}$), shown in Figure 1(c), and the transverse momentum of the $t\bar{t}$ system, shown in Figure 1(d). The transverse momenta of the hadronically decaying top quark and the $t\bar{t}$ system are obtained after the event reconstruction described in Section 4.4 is performed. The distributions of transverse momenta predicted by the MC simulation, e.g. the $p_{\text{T,had}}$ distribution shown in Figure 1(c), show a slightly different trend

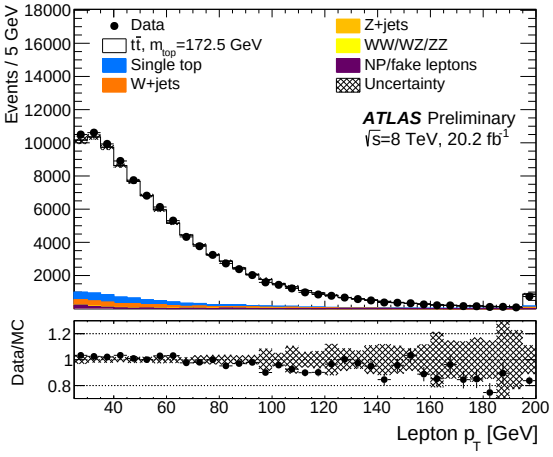

(a) Lepton transverse momentum

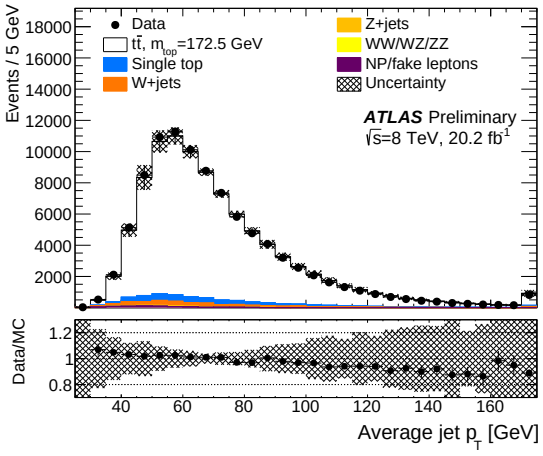

(b) Average jet transverse momentum

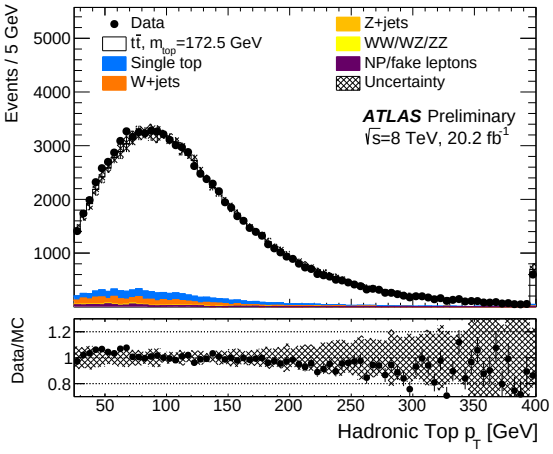

(c) Hadronic top quark transverse momentum

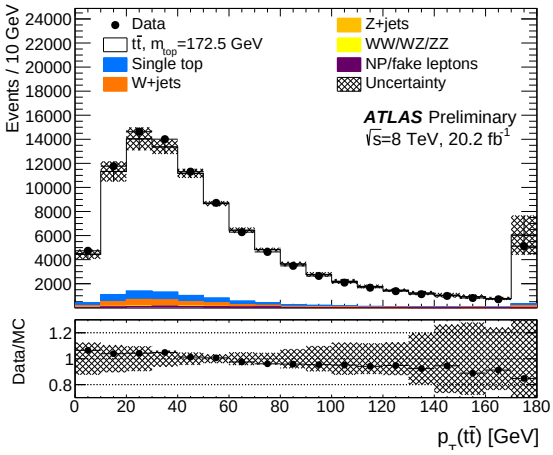

(d) Transverse momentum of the $t\bar{t}$ system

Figure 1: Distributions for the selected events passing the event preselection. The data are shown (black points) together with the signal-plus-background prediction (solid histogram), normalised to the number of events observed in the data. The hatched area is the uncertainty on the prediction as described in the text. The rightmost bin also contains the overflow if present. Figure (a) shows the transverse momentum of the lepton, figure (b) the average transverse momentum of the jets, figure (c) the transverse momentum of the hadronically decaying top quark, and finally, figure (d) the transverse momentum of the $t\bar{t}$ system.

than what is observed in data, with the data being softer. This difference is however fully covered by the uncertainties. This trend was already observed in Ref. [14] for the $p_{T,\ell b}$ distribution in the $t\bar{t} \to$ dilepton channel and in the measurement of the differential $t\bar{t}$ cross-section in the lepton+jets channel [71].

4.4 Reconstruction of the three observables

To measure the top quark mass, a full reconstruction of the event is performed using a kinematic reconstruction based on a likelihood fit performed with the KLFitter package [72, 73].

The KLFitter algorithm relates the measured kinematics of the reconstructed objects to the leading-order representation of the $t\bar{t}$ system decay, using $t\bar{t} \to \ell\nu b_{\text{lep}}\, q_1 q_2 b_{\text{had}}$. In this procedure, the measured jets relate to the quark decay products of the W boson, q_1 and q_2, and to the b-quarks, b_{lep} and b_{had}, produced in the leptonic and hadronic top quark decays.

The event likelihood is constructed as the product of Breit–Wigner (BW) distributions and transfer functions (TFs). The W boson BW line-shape functions use the world combined values of the W boson mass and decay width from Ref. [3]. A common mass parameter, $m_{\text{top}}^{\text{reco}}$, is used for the BW distributions describing the leptonically and hadronically decaying top quarks, and this is fitted event-by-event. The top quark width varies with $m_{\text{top}}^{\text{reco}}$ and is calculated according to the SM prediction [3]. The TFs are derived from the Powheg+Pythia $t\bar{t}$ signal MC simulation sample at an input mass of $m_{\text{top}} = 172.5$ GeV. They represent the experimental resolutions in terms of the probability that the observed energy at reconstruction level is produced by a given parton-level object for the leading-order decay topology, and are used in the fit to constrain the variations of the reconstructed objects.

The settings of the reconstruction algorithm were optimised compared to Ref. [9], achieving a larger fraction of correct assignments of reconstructed jets to partons from the $t\bar{t} \to$ lepton + jets decay. The input objects to the likelihood are: the reconstructed charged lepton, the missing transverse momentum and up to six jets. These are the two b-tagged jets and the four untagged jets with the highest p_{T}. The x- and y-components of the missing transverse momentum are used as starting values for the neutrino transverse-momentum components, with its longitudinal component ($p_{\nu,z}$) as a free parameter in the kinematic likelihood fit. Its starting value is computed from the $W \to \ell\nu$ mass constraint. If there are no real solutions for $p_{\nu,z}$ a starting value of zero is used. If there are two real solutions, the one giving the largest likelihood value is taken.

Maximising the event-by-event likelihood as a function of $m_{\text{top}}^{\text{reco}}$ establishes the best assignment of reconstructed jets to partons from the $t\bar{t} \to$ lepton + jets decay. The maximisation is performed by testing all possibilities for assigning b-tagged jets to b-quark positions and untagged jets to light quark positions. The value of $m_{\text{top}}^{\text{reco}}$ obtained from the kinematic likelihood fit is used as the observable primarily sensitive to the underlying m_{top}. The invariant mass of the hadronically decaying W boson (m_W^{reco}) is calculated from the assigned jets of the chosen permutation. Finally, an observable called R_{bq}^{reco}, designed to be sensitive to the relative b-to-light-jet energy scale, is computed as the scalar sum of the transverse momenta of the two b-tagged jets divided by the scalar sum of the transverse momenta of the two jets associated with the hadronic W boson decay:

$$R_{bq}^{\text{reco}} = \frac{p_{\text{T}}^{b_{\text{had}}} + p_{\text{T}}^{b_{\text{lep}}}}{p_{\text{T}}^{q_1} + p_{\text{T}}^{q_2}} \,. \tag{1}$$

The values of m_W^{reco} and R_{bq}^{reco} are computed from the jet four-vectors as given by the jet reconstruction instead of using the values obtained in the kinematic likelihood fit. This ensures the maximum sensitivity to changes of the jet energy scale for light jets and b-jets.

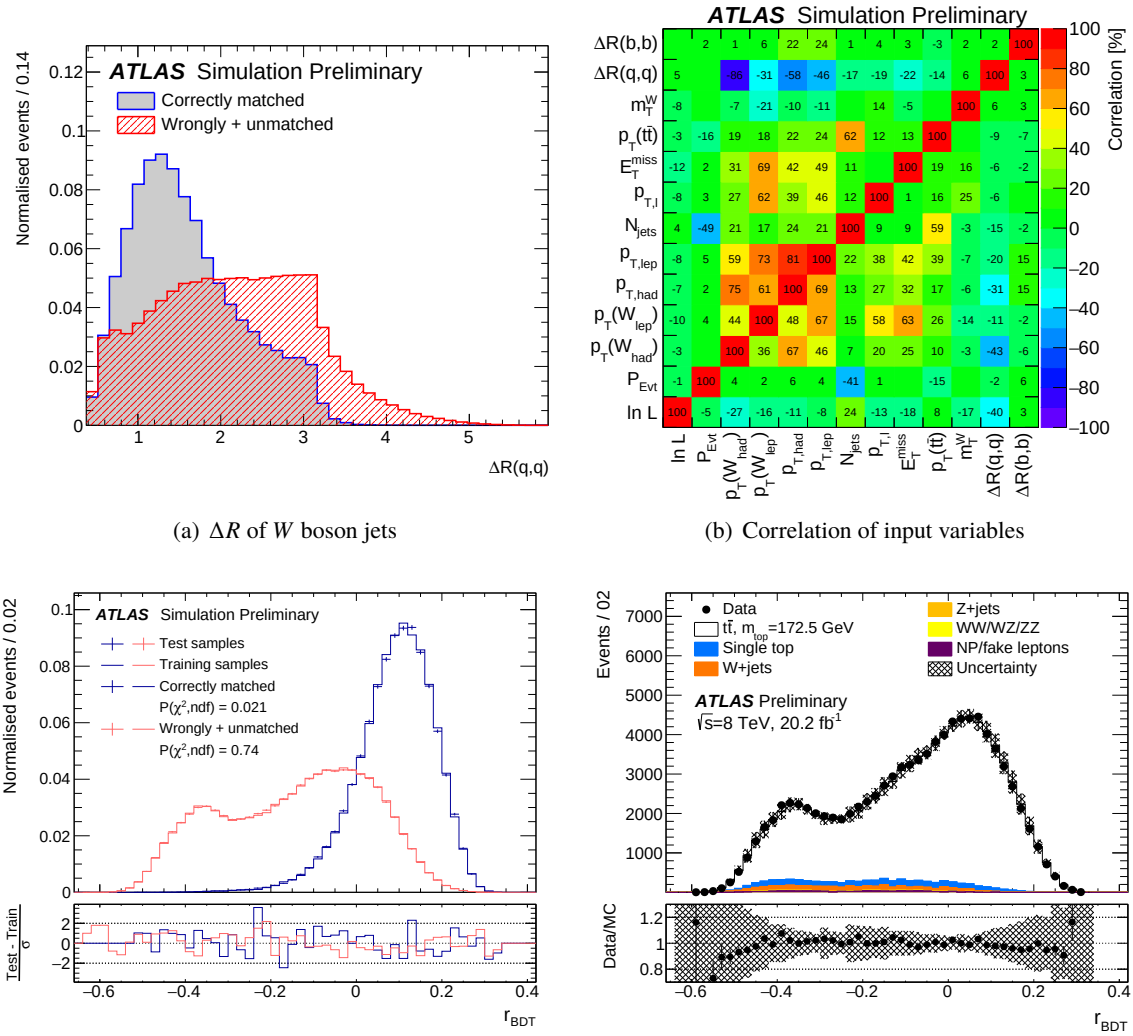

(a) ΔR of W boson jets

(b) Correlation of input variables

(c) BDT test and training samples

(d) Data-to-MC comparison for r_{BDT}

Figure 2: Input and results of the BDT training on $t\bar{t}$ signal. Figure (a) shows the distribution of the ΔR between the two untagged jets assigned to the W boson decay for the correctly matched events and the remainder. Figure (b) shows the correlation of the input variables to the BDT algorithm for the correctly matched events above the diagonal, and those for the remaining events below. Figure (c) shows the BDT response r_{BDT} for the two classes of events for both the training and the test samples with statistical uncertainties. The compatibility in terms of the χ^2 probability is also listed. Finally, figure (d) shows the comparison of the r_{BDT} distribution observed in data and MC simulation. The hatched area includes the uncertainties as detailed in the text. The uncertainty bars correspond to the statistical uncertainties in the data.

5 Multivariate analysis and BDT event selection

For the measurement of m_{top}, the event preselection is refined based on the assumption that events with correct assignments of reconstruction-level objects to their generator-level counterparts are better measured and should therefore lead to smaller uncertainties. The optimisation of the selection is based on a multivariate algorithm, namely a boosted decision tree (BDT), as implemented in the TMVA package [74].

Separation	Variable	Description
31%	$\ln L$	Logarithm of the likelihood of best permutation
13%	$\Delta R(q, q)$	ΔR of the two untagged jets from the hadronically decaying W boson
5.0%	$p_{\mathrm{T}}(W_{\mathrm{had}})$	p_{T} of hadronically decaying W boson
4.3%	$p_{\mathrm{T,had}}$	p_{T} of hadronically decaying top quark
4.2%	P_{Evt}	Event probability of best permutation
2.0%	$p_{\mathrm{T}}(t\bar{t})$	p_{T} of reconstructed $t\bar{t}$ system
1.7%	$p_{\mathrm{T,lep}}$	p_{T} of leptonically decaying top quark
1.2%	m_{T}^{W}	Transverse mass of leptonically decaying W boson
0.3%	$p_{\mathrm{T}}(W_{\mathrm{lep}})$	p_{T} of leptonically decaying W boson
0.3%	N_{jets}	Number of jets
0.2%	$\Delta R(b, b)$	ΔR of reconstructed b-tagged jets
0.2%	$E_{\mathrm{T}}^{\mathrm{miss}}$	Missing transverse momentum
0.1%	$p_{\mathrm{T},\ell}$	p_{T} of lepton

Table 2: The input variables to the BDT algorithm sorted by their separation power. All variables are output variables of the KLFitter package, except for N_{jets}, $E_{\mathrm{T}}^{\mathrm{miss}}$, m_{T}^{W} and $p_{\mathrm{T},\ell}$.

To estimate the performance of this algorithm in MC simulated samples, the reconstruction-level objects are matched to the closest parton-level object based on a maximum allowed ΔR, being 0.1 for leptons and 0.3 for jets. A matched object is defined as a reconstruction-level object that falls within ΔR of any parton-level object of that type, and a correct match means that this generator-level object is the one it originated from. Due to acceptance losses and reconstruction inefficiency, not all reconstruction-level objects can successfully be matched to their parton-level counterparts. If not all partons can be unambiguously matched to a jet, the corresponding event is referred to as *unmatched*. The matching efficiency is the fraction of correctly matched events among all the matched events, and the selection purity is the fraction of correctly matched events among all events, regardless of whether they could be matched or not.

The BDT algorithm is used to separate events with a correct jet-to-parton matching from the remainder, i.e. the sum of wrongly matched and unmatched events. Given that the BDT optimisation utilises the matching, it is solely based on the $t\bar{t}$ signal sample at $m_{\mathrm{top}} = 172.5$ GeV. However, the variables are chosen such that the BDT output can be calculated for any event. Many variables were studied and only those with a separation power larger than 0.1% were used in the training[5]. The thirteen variables chosen for the final training are given in Table 2. The largest separation power for the two classes of events is contained in the likelihood of the chosen permutation and the opening angle ΔR of the two untagged jets associated with the W boson decay. For all thirteen input variables to the BDT algorithm a good agreement of the MC prediction with data is found.

As an example of the input distributions to the BDT algorithm, the ΔR of the two untagged jets assigned to the W boson decay is shown in Figure 2(a). The correlations in percent of all input variables are shown in Figure 2(b), where the correlations for the correctly matched events are shown above the diagonal, and those for the remaining events below. The observed differences for the two classes of events are exploited by the BDT algorithm. Half the MC simulation sample is used to train the algorithm, the other half to assess its performance. The significant difference of the r_{BDT} distributions between the

[5] The definition of the *separation power* is used as introduced in Equation 1 of the TMVA manual [74].

two classes of events in Figure 2(c) shows their efficient separation by the BDT algorithm. In addition, reasonable agreement is found for the r_{BDT} distributions in the statistically independent test and training samples. Finally, the r_{BDT} distributions in MC simulation and data shown in Figure 2(d) agree within the experimental uncertainties. This justifies the application of the BDT approach to the data.

The full m_{top} analysis is performed for several selection requirements on r_{BDT} to find the point of smallest total uncertainty. In addition, in view of the template parameterisation described in Section 6 the following restrictions on the three observables are applied: $m_{\mathrm{top}}^{\mathrm{reco}} \in [125, 200]$ GeV, $m_{W}^{\mathrm{reco}} \in [55, 110]$ GeV, and $R_{bq}^{\mathrm{reco}} \in [0.3, 3.0]$. Since only the best permutation is considered in this analysis, events that do not pass these requirements are rejected. These requirements remove events in the tails of the three distributions, which are typically poorly reconstructed with small likelihood values and do not contain significant information on m_{top}. Consequently, the templates then have simpler shapes which are easier to model analytically with fewer parameters. The preselection with these additional requirements is referred to as the *standard selection*, to distinguish it from the following BDT optimisation in search for the smallest total uncertainty in m_{top}.

Using additional selection cuts on the value of r_{BDT} in the range of $[-0.10, 0.05]$ in steps of 0.05, the optimisation is performed separately for the sample with at least one b-tagged jet and the sample with two b-tagged jets. The latter results in smaller uncertainties and therefore the sample with two b-tagged jets is chosen for the m_{top} analysis. The value of $r_{\mathrm{BDT}} = -0.05$ provides the smallest total uncertainty in m_{top}.

The resulting numbers of events for this *BDT selection* are given in Table 1. Compared to the preselection, the efficiency for correctly matched events is increased from 0.71 to 0.82, albeit at the expense of a significant reduction in the number of selected events. In addition, the intrinsic resolution in m_{top} of the remaining event sample is improved, i.e. it does not scale with the square root of the number of events retained. Some distributions of the observed event kinematics are shown in Figure 3. Similar to the distributions shown for the preselection in Figure 1, good agreement of the MC prediction with data is found. This is shown for the observed W boson transverse mass for the leptonically decaying top quark, Figure 3(a), and for the three observables of the m_{top} analysis, Figures 3(b)–3(d). The sharp edge observed at 30 GeV in Figure 3(a) originates from the different selection requirements for the W boson transverse mass in the electron and muon channels.

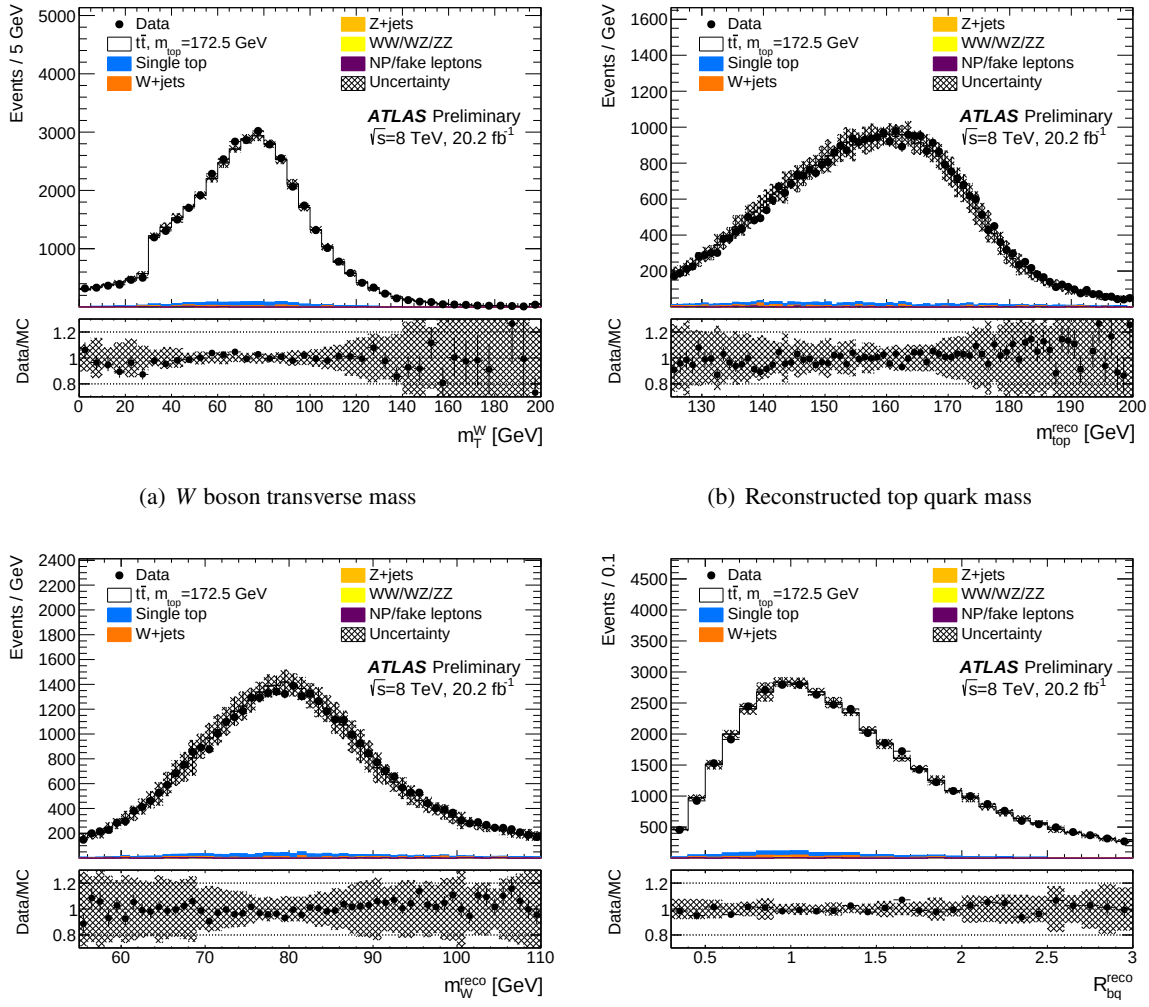

(a) W boson transverse mass

(b) Reconstructed top quark mass

(c) Reconstructed W boson mass

(d) Reconstructed ratio of jet transverse momenta

Figure 3: Distributions for the selected events passing the BDT event selection. The data are shown (black points), together with the signal-plus-background prediction (solid histogram) normalised to the number of events observed in the data. The hatched area is the uncertainty in the prediction described in the text. The rightmost bin also contains the overflow if present. Figure (a) shows the W boson transverse mass for the leptonic top quark decay. The remaining figures show the three observables used for the determination of m_{top}, where figure (b) shows the reconstructed top quark mass $m_{\text{top}}^{\text{reco}}$, figure (c) the reconstructed invariant mass of the W boson m_{W}^{reco}, and finally figure (d) the reconstructed ratio of jet transverse momenta R_{bq}^{reco}.

6 Template fit

This analysis uses a three-dimensional template fit technique which determines m_{top} together with JSF and bJSF. The aim of the multi-dimensional fit to the data is to measure m_{top} and, at the same time, to absorb the mean differences between the jet energy scales observed in data and simulated events into jet energy scale factors. Using JSF and bJSF, most of the uncertainties in m_{top} induced by JES and bJES uncertainties are transformed into additional statistical components caused by the higher dimensionality of the fit. Only for sufficiently large data samples does this method pay off. For this situation, the sum in quadrature of the additional statistical uncertainty in m_{top} due to the JSF (or bJSF) fit and the residual JES (or bJES) induced systematic uncertainty is smaller than the original JES (or bJES) induced uncertainty in m_{top}. This situation was already realised for the 7 TeV analysis [9], and is even more advantageous for the much larger data sample of the 8 TeV analysis. Since JSF and bJSF are global factors, they do not completely absorb the JES and bJES uncertainties which have p_{T}- and η-dependent components.

For simultaneously determining m_{top}, JSF and bJSF, templates are constructed from the MC samples. Templates of $m_{\text{top}}^{\text{reco}}$ are constructed as a function of the m_{top} used in the MC simulation in the range 167.5–177.5 GeV, with independent input values for JSF and bJSF in the range 0.96–1.04. Statistically independent MC samples are used for different input values of m_{top}. From those samples, templates with different values of JSF and bJSF are constructed by scaling the energies of the jets in each sample appropriately. JSF is applied to all jets, while bJSF is solely applied to b-jets according to the information about the generated quark flavour. The scaling is performed after the various correction steps of the jet calibration, but before the event selection. This procedure results in different events entering the BDT selection from one energy scale variation to another. However, many events are in all samples, resulting in a large statistical correlation of the samples with different jet scale factors. Similarly, templates of m_W^{reco} and R_{bq}^{reco} are constructed as functions of the input values of m_{top}, JSF and bJSF.

Signal templates are derived for the three observables for all m_{top}-dependent samples, consisting of the $t\bar{t}$ signal events and single-top-quark production events. This procedure is adopted because single-top-quark production, although formally a background process, still carries information about the top quark mass. In addition, m_{top}-independent background templates can then be used. The signal templates are fitted to the sum of a Gaussian and two Landau functions for $m_{\text{top}}^{\text{reco}}$, to the sum of two Gaussian functions for m_W^{reco}, and to the sum of two Gaussian and one Landau function for R_{bq}^{reco}. For the background, the $m_{\text{top}}^{\text{reco}}$ distribution is fitted to a Landau function, while both the m_W^{reco} and the R_{bq}^{reco} distributions are fitted to the sum of two Gaussian functions.

In Figures 4(a)–4(c), the sensitivity of $m_{\text{top}}^{\text{reco}}$ to the fit parameters m_{top}, JSF and bJSF is shown by the superposition of the signal templates and their fits for three input values per varied parameter. In a similar way, the sensitivity of m_W^{reco} to JSF is shown in Figure 4(d). The dependence of m_W^{reco} on the input values of m_{top} and bJSF is found to be negligible. Consequently, to increase the size of the MC simulation sample used, the fit is performed to the sum of the m_W^{reco} distributions of the samples with different input top quark masses. Finally, the sensitivity of R_{bq}^{reco} on the input values of m_{top} and bJSF is shown in Figures 4(e)–4(f). The dependence of R_{bq}^{reco} on JSF (not shown) is found to be much weaker than the dependence on bJSF.

For the signal, the parameters of the fitting functions for $m_{\text{top}}^{\text{reco}}$ depend linearly on m_{top}, JSF and bJSF. The parameters of the fitting functions for m_W^{reco} depend linearly on JSF. Finally, the parameters of the fitting functions for R_{bq}^{reco} depend linearly on m_{top}, JSF and bJSF. For the background, the dependences of the parameters of the fitting functions are identical to those for the signal, except for the fact that they do not depend on m_{top}, and that those for R_{bq}^{reco} do not depend on JSF.

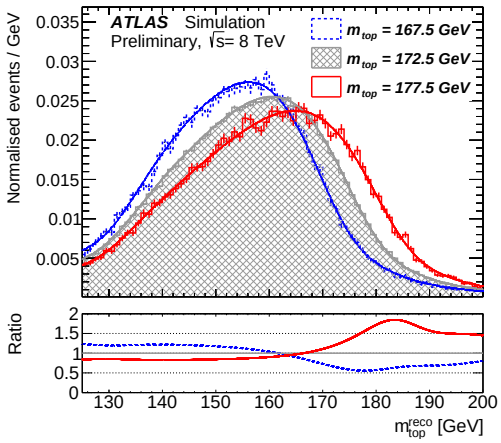

(a) $m_{\text{top}}^{\text{reco}}$ as a function of m_{top}

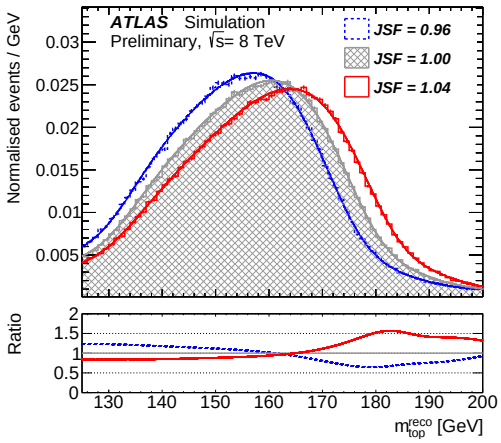

(b) $m_{\text{top}}^{\text{reco}}$ as a function of JSF

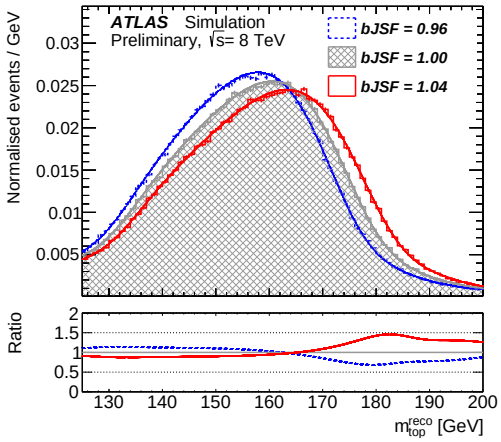

(c) $m_{\text{top}}^{\text{reco}}$ as a function of bJSF

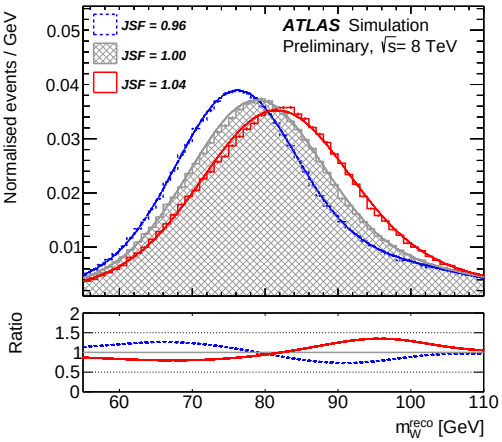

(d) m_{W}^{reco} as a function of JSF

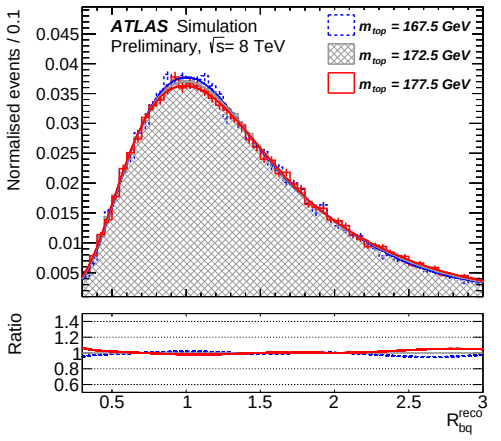

(e) R_{bq}^{reco} as a function of m_{top}

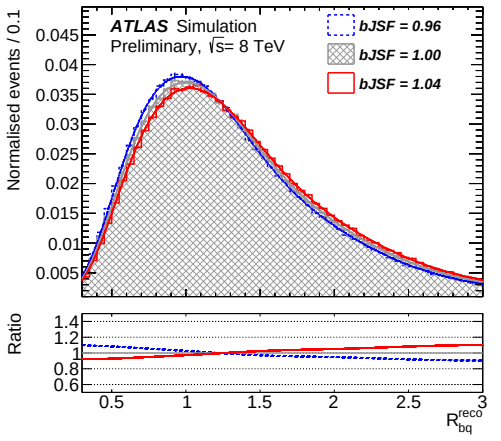

(f) R_{bq}^{reco} as a function of bJSF

Figure 4: Template parametrisations for signal events, composed of $t\bar{t}$ and single-top-quark production events. Figures (a-c) show the sensitivity of $m_{\text{top}}^{\text{reco}}$ to m_{top}, JSF, and bJSF, figure (d) shows the sensitivity of m_{W}^{reco} to JSF, and finally, figures (e, f) show the sensitivity of R_{bq}^{reco} to m_{top}, and bJSF. Each template is overlaid with the corresponding probability density function (pdf) from the combined fit to all templates. The ratio shown in the lower panel is calculated with respect to the central sample pdf, displayed with the hatched area.

Signal and background probability density functions $P_{\text{top}}^{\text{sig}}$ and $P_{\text{top}}^{\text{bkg}}$ for the $m_{\text{top}}^{\text{reco}}$, m_W^{reco} and R_{bq}^{reco} distributions are used in an unbinned likelihood fit to the data for all events, $i = 1, \ldots N$. The likelihood function maximised is:

$$\begin{aligned} L_{\text{shape}}^{\ell+\text{jets}}(m_{\text{top}}, \text{JSF}, \text{bJSF}, f_{\text{bkg}}) = \prod_{i=1}^{N} & P_{\text{top}}(m_{\text{top}}^{\text{reco,i}} \,|\, m_{\text{top}}, \text{JSF}, \text{bJSF}, f_{\text{bkg}}) \\ & \times P_{\text{W}}(m_W^{\text{reco,i}} \,|\, \text{JSF}, f_{\text{bkg}}) \\ & \times P_{\mathcal{R}_{\text{bq}}}(R_{bq}^{\text{reco,i}} \,|\, m_{\text{top}}, \text{JSF}, \text{bJSF}, f_{\text{bkg}}), \end{aligned} \tag{2}$$

with:

$$\begin{aligned} P_{\text{top}}(m_{\text{top}}^{\text{reco,i}} \,|\, m_{\text{top}}, \text{JSF}, \text{bJSF}, f_{\text{bkg}}) &= (1 - f_{\text{bkg}}) \cdot P_{\text{top}}^{\text{sig}}(m_{\text{top}}^{\text{reco,i}} \,|\, m_{\text{top}}, \text{JSF}, \text{bJSF}) + \\ &\quad f_{\text{bkg}} \cdot P_{\text{top}}^{\text{bkg}}(m_{\text{top}}^{\text{reco,i}} \,|\, \text{JSF}, \text{bJSF}) \,, \\ P_{\text{W}}(m_W^{\text{reco,i}} \,|\, \text{JSF}, f_{\text{bkg}}) &= (1 - f_{\text{bkg}}) \cdot P_{\text{W}}^{\text{sig}}(m_W^{\text{reco,i}} \,|\, \text{JSF}) + \\ &\quad f_{\text{bkg}} \cdot P_{\text{W}}^{\text{bkg}}(m_W^{\text{reco,i}} \,|\, \text{JSF}) \,, \\ P_{\mathcal{R}_{\text{bq}}}(R_{bq}^{\text{reco,i}} \,|\, m_{\text{top}}, \text{JSF}, \text{bJSF}, f_{\text{bkg}}) &= (1 - f_{\text{bkg}}) \cdot P_{\mathcal{R}_{\text{bq}}}^{\text{sig}}(R_{bq}^{\text{reco,i}} \,|\, m_{\text{top}}, \text{JSF}, \text{bJSF}) + \\ &\quad f_{\text{bkg}} \cdot P_{\mathcal{R}_{\text{bq}}}^{\text{bkg}}(R_{bq}^{\text{reco,i}} \,|\, \text{bJSF}) \,. \end{aligned}$$

where the fraction of background events is denoted by f_{bkg}. The parameters determined by the fit are m_{top}, JSF and bJSF, while f_{bkg} is fixed to its expectation shown in Table 1. It has been verified that the correlations between $m_{\text{top}}^{\text{reco}}$, m_W^{reco} and R_{bq}^{reco} are small enough that formulating the likelihood as a product of three one-dimensional likelihoods does not create a bias in the result.

Pseudo-experiments are used to verify the internal consistency of the fitting procedure and to obtain the expected statistical uncertainty for the data. For each set of parameter values, 500 pseudo-experiments are performed, each corresponding to the integrated luminosity of the data. To retain the correlation of the three observables for the three-dimensional fit, individual events are used. Because this exceeds the available MC statistics, results are corrected for oversampling [75], if appropriate. The results of pseudo-experiments for different input values of m_{top} are obtained from statistically independent samples, while the results for different JSF and bJSF are obtained from correlated samples as explained above. For each fitted quantity and each variation of input parameters, the residual, i.e. the difference of the input value and the value obtained by the fit, is consistent with zero. The three expected statistical uncertainties amount to:

$$\begin{aligned} \sigma_{\text{stat}}(m_{\text{top}}) &= 0.389 \quad \pm 0.004 \text{ GeV}, \\ \sigma_{\text{stat}}(\text{JSF}) &= 0.00115 \pm 0.00001\,, \\ \sigma_{\text{stat}}(\text{bJSF}) &= 0.0046 \quad \pm 0.0001\,, \end{aligned}$$

where the values quoted are the mean and RMS of the distribution of the statistical uncertainties in the fitted quantities from pseudo-experiments. The widths of the pull distributions are below unity for m_{top} and the two jet scale factors, which results in an overestimation of the uncertainty in m_{top} of up to 7%. Since this leads to a conservative estimate of the uncertainty in m_{top}, no attempts to mitigate this feature are made.

	m_{top} [GeV]		
	$\sqrt{s}$ = 7 TeV	$\sqrt{s}$ = 8 TeV	
Event selection	Standard	Standard	BDT
Result	172.33	171.90	172.08
Statistics	0.75	0.38	0.39
– *Stat. comp. (m_{top})*	0.23	0.12	0.11
– *Stat. comp. (*JSF*)*	0.25	0.11	0.11
– *Stat. comp. (*bJSF*)*	0.67	0.34	0.35
Method	0.11 ± 0.10	0.04 ± 0.11	0.13 ± 0.11
Signal Monte Carlo generator	0.22 ± 0.21	0.50 ± 0.17	0.16 ± 0.17
Hadronisation	0.18 ± 0.12	0.05 ± 0.10	0.15 ± 0.10
Initial- and final-state QCD radiation	0.32 ± 0.06	0.28 ± 0.11	0.08 ± 0.11
Underlying event	0.15 ± 0.07	0.08 ± 0.15	0.08 ± 0.15
Colour reconnection	0.11 ± 0.07	0.37 ± 0.15	0.19 ± 0.15
Parton distribution function	0.25 ± 0.00	0.08 ± 0.00	0.09 ± 0.01
Background normalisation	0.10 ± 0.00	0.04 ± 0.00	0.08 ± 0.00
W+jets shape	0.29 ± 0.00	0.05 ± 0.00	0.11 ± 0.00
Fake leptons shape	0.05 ± 0.00	0	0
Jet energy scale	0.58 ± 0.11	0.63 ± 0.02	0.54 ± 0.02
Relative b-to-light-jet energy scale	0.06 ± 0.03	0.05 ± 0.01	0.03 ± 0.01
Jet energy resolution	0.22 ± 0.11	0.23 ± 0.03	0.20 ± 0.04
Jet reconstruction efficiency	0.12 ± 0.00	0.04 ± 0.01	0.02 ± 0.01
Jet vertex fraction	0.01 ± 0.00	0.13 ± 0.01	0.09 ± 0.01
b-tagging	0.50 ± 0.00	0.37 ± 0.00	0.38 ± 0.00
Leptons	0.04 ± 0.00	0.16 ± 0.01	0.16 ± 0.01
$E_{\text{T}}^{\text{miss}}$	0.15 ± 0.04	0.08 ± 0.01	0.05 ± 0.01
Pile-up	0.02 ± 0.01	0.14 ± 0.01	0.15 ± 0.01
Total systematic uncertainty	1.03 ± 0.08	1.07 ± 0.10	0.82 ± 0.06
Total	1.27 ± 0.08	1.13 ± 0.10	0.91 ± 0.06

Table 3: Systematic uncertainties in m_{top}. The measured values of m_{top} are given together with the statistical and systematic uncertainty components for the standard and the BDT event selections. For each systematic uncertainty listed, the first value corresponds to the uncertainty in m_{top}, and the second to the statistical precision of this uncertainty. An integer value of zero means that the corresponding uncertainty is negligible and therefore not evaluated. If the statistical precision of the uncertainty is smaller than 0.005, the statistical precision is displayed as 0.00. For comparison, the result in the $t\bar{t} \to$ lepton + jets channel at $\sqrt{s}$ = 7 TeV from Ref. [9] is also listed. The last line refers to the sum in quadrature of the statistical and systematic uncertainties.

7 Uncertainties affecting the m_{top} determination

This section focusses on the treatment of uncertainty sources of a systematic nature. The same systematic uncertainty sources as in Ref. [9] are investigated. If possible, their impact on the analysis is evaluated by varying the respective quantities by $\pm 1\sigma$ with respect to their default values, constructing the corresponding template and measuring the average m_{top} change with respect to the result from the nominal MC sample with 500 pseudo-experiments each, drawn from the full MC sample. In the absence of a $\pm 1\sigma$ variation, e.g. for the evaluation of the uncertainty induced by the choice of signal MC generator, the full observed difference is assigned as a symmetric systematic uncertainty and further treated as a variation equivalent to a $\pm 1\sigma$ variation. Wherever a $\pm 1\sigma$ variation can be performed, half the observed difference between the $+1\sigma$ and -1σ variation in m_{top} is assigned as an uncertainty if the variations lie on opposite sides of the

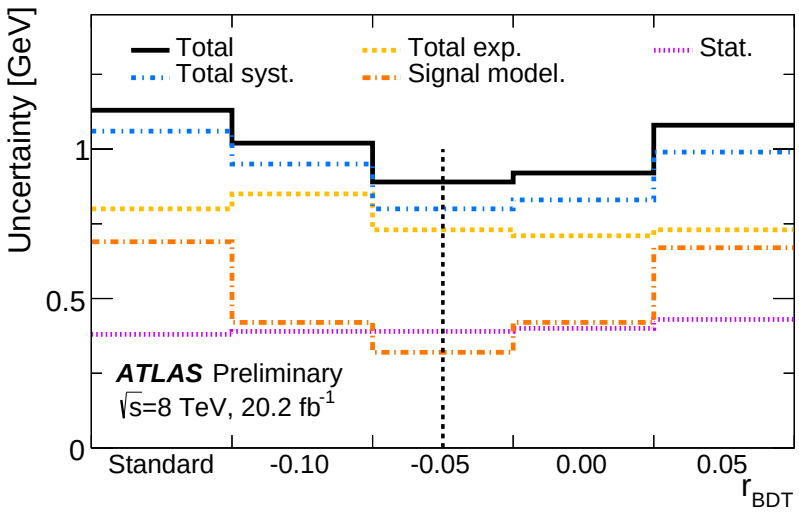

Figure 5: Various classes of uncertainties as function of the BDT working point r_{BDT}. The total uncertainty (black solid line) is the quadratic sum of the statistical (dotted purple line) and total systematic uncertainty (dash-dotted blue line). The total systematic uncertainty consists of the total experimental (dashed yellow line) and total signal modelling uncertainty (dash-dotted orange line). The uncertainties on the background estimate are included in the total experimental uncertainty. The chosen working point is indicated by the vertical black dashed line. All uncertainties except for the method and the pile-up uncertainties are included.

nominal result. If they lie on the same side, the full maximum observed difference is taken as a symmetric systematic uncertainty. To facilitate a combination with other results, every systematic uncertainty is assigned a statistical uncertainty, taking into account the statistical correlation of the considered samples, as explained in Section 7.5. The resulting uncertainty components are given in Table 3 irrespective of their statistical significance. This approach follows the suggestion in Ref. [76] and relies on the fact that, given a large enough number of considered uncertainty sources, statistical fluctuations average out. The uncertainty sources are constructed such as to be uncorrelated with each another and thus the total uncertainty squared is calculated as the sum in quadrature of all components. The individual uncertainties are compared in Table 3 for three cases: the standard selection for the $\sqrt{s} = 7$ TeV [9] and 8 TeV data, and the BDT selection for 8 TeV data. Many uncertainties in m_{top} obtained with the standard selection at the two centre-of-mass energies agree within their statistical uncertainties such that the resulting total systematic uncertainties are almost identical. Consequently, repeating the $\sqrt{s} = 7$ TeV analysis on $\sqrt{s} = 8$ TeV data would have only improved on the statistical precision.

The picture changes when comparing the uncertainties on $\sqrt{s} = 8$ TeV data for the standard selection and the BDT selection. In general, the experimental uncertainties change only slightly, with the largest reduction observed for the JES uncertainty. In contrast, a large improvement comes from the reduced uncertainties in the modelling of the $t\bar{t}$ signal processes as shown in Table 3. This, together with the improved intrinsic resolution in m_{top}, more than compensates the small loss in precision caused by the increased statistical uncertainty. The evolution of the statistical and systematic uncertainties as function of r_{BDT} is shown in Figure 5. The individual sources of systematic uncertainties and the evaluation of their effect on m_{top} are described in the following.

7.1 Statistics and method calibration

Uncertainties related to statistical effects and the method calibration are discussed here.

Statistical: The quoted statistical uncertainty consists of three parts: a purely statistical component in m_{top} and the contributions stemming from the simultaneous determination of JSF and bJSF. The purely statistical component in m_{top} is obtained from a one-dimensional template method exploiting only the $m_{\text{top}}^{\text{reco}}$ observable, while fixing the values of JSF and bJSF to the results of the three-dimensional analysis. The contribution to the statistical uncertainty in the fitted parameters due to the simultaneous fit of m_{top} and JSF is estimated as the difference in quadrature between the statistical uncertainty of a two-dimensional fit to $m_{\text{top}}^{\text{reco}}$ and m_{W}^{reco}, while fixing the value of bJSF, and the one-dimensional fit to the data described above. Analogously, the contribution of the statistical uncertainty due to the simultaneous fit of m_{top} together with JSF and bJSF is defined as the difference in quadrature between the statistical uncertainties obtained in the three-dimensional and the two-dimensional fits to the data. This separation allows a direct comparison of the sensitivity of the m_{top} estimator for any analysis, irrespective of the number of observables exploited by the fit. In addition, the sensitivity of the estimators to the global jet energy scales can be directly compared. These uncertainties are treated as uncorrelated uncertainties in m_{top} combinations. Together with the systematic components of the residual jet energy scale uncertainties discussed below, they directly replace the uncertainty in m_{top} from the jet energy scale variations present without the in-situ determination.

Method: The residual difference between fitted and generated m_{top} when analysing a template from a MC sample reflects the potential bias of the method. Consequently, the largest observed fitted m_{top} residual and the largest observed statistical uncertainty in this quantity is assigned as the method calibration uncertainty and its corresponding statistical uncertainty, respectively. This also covers effects from limited numbers of MC simulated events in the templates and potential deficiencies in the template parameterisations.

7.2 Modelling of signal processes

The $t\bar{t} \rightarrow$ lepton + jets events have a rich physics environment and are consequently subject to various systematic effects, ranging from the $t\bar{t}$ production to the hadronisation of the showered objects.

Thanks to the restrictive event selection requirements, the contribution of non-$t\bar{t}$ processes, comprising the single-top-quark process and the various background processes, is very low. The impact of varying the single-top-quark normalisation is estimated from the corresponding uncertainty in the theoretical cross-section given in Section 3. The resulting systematic uncertainty is found to be small compared to the systematic uncertainty in the $t\bar{t}$ production that accounts for most of the signal events, and is consequently neglected. For the modelling of the signal processes, the impact of including single-top variations in the uncertainty evaluation has been tested for various uncertainty sources and was also found to be negligible. Therefore the single-top-quark variations are not included in the determination of the signal event uncertainties.

Signal Monte Carlo generator: The difference in m_{top} between the event sample produced with the MC@NLO program [77, 78] and the default Powheg-Box sample is quoted as a systematic uncertainty. Both samples are generated with a top quark mass of $m_{\text{top}} = 172.5$ GeV, use the CT10 PDFs in the ME calculation and are using the Herwig and Jimmy programs with the ATLAS AUET2 tune [45]. The functional form of the renormalisation and factorisation scales depends on the transverse momenta of the top and anti-top as well as the top quark mass:

$$\mu_{\text{F,R}} = \sqrt{\frac{p_{\text{T,t}}^2 + p_{\text{T,}\bar{\text{t}}}^2}{2} + m_{\text{top}}^2} \, . \tag{3}$$

Hadronisation: To cover the choice of the parton shower and hadronisation model, samples produced with the Powheg-Box program are showered with either the Pythia6 program using the P2011C tune or the Herwig and Jimmy programs using the ATLAS AUET2 tune [45]. This includes different approaches in shower modelling, like the usage of a p_{T}-ordered PS in the Pythia program or angular-ordered PS in the Herwig program, the different PS matching scales, as well as fragmentation functions and hadronisation models like the choice of the Lund string model [79, 80], implemented in the Pythia program, or the cluster fragmentation model [81] used in the Herwig program. The full observed difference between the samples is quoted as a systematic uncertainty.

As shown in Figure 1, the distributions of transverse momenta in data are slightly softer than those in the Powheg+Pythia MC simulation samples. Similarly to what was observed in the $t\bar{t} \to$ dilepton channel for the $p_{T,\ell b}$ distribution, in the $t\bar{t} \to$ lepton + jets channel the Powheg+Herwig sample is much closer to the data for several distributions of transverse momenta. The $p_{\text{T,had}}$ distribution is much better described by the Powheg+Herwig sample, as also observed in Ref. [71]. In addition, but to a lesser extent, the MC@NLO sample used to assess the signal Monte Carlo generator uncertainty, and the samples to assess the ISR/FSR uncertainty discussed next, also lead to a softer distribution in simulation. Given this, the observed difference in the $p_{\text{T,had}}$ distribution is covered by a combination of the signal modelling uncertainties given in Table 3.

The jet energy response is defined as the ratio of reconstruction-level jet p_{T} to stable-particle-level jet p_{T}. The response typically ranges from 0.5 to 0.9, due to energy-loss effects like out-of-cone radiation dominating over energy-gain effects like pile-up. Despite the fact that the JES and bJES are estimated independently using dijet and other non-$t\bar{t}$ samples [61], a certain level of double-counting of hadronisation uncertainty induced uncertainties in the JES and m_{top} cannot be excluded. This was investigated closely for the ATLAS top quark mass measurement in the $t\bar{t} \to$ lepton + jets channel at $\sqrt{s} = 7$ TeV. The results in Ref. [82] revealed that the amount of double-counting of JES and hadronisation effects for the $t\bar{t} \to$ lepton + jets channel is small.

Initial and Final State QCD Radiation (ISR/FSR): Adding ISR/FSR on top of the matrix element leads to a higher jet multiplicity and different jet energies in the event, which affects the distributions of the three observables. The uncertainties due to ISR/FSR modelling are estimated with samples generated with Powheg-Box interfaced to the Pythia6 program for which the parameters of the generation are varied to span the ranges compatible with the results of measurements of $t\bar{t}$ production in association with jets [83–85]. The effect is evaluated by comparing two dedicated samples that differ in several parameters, namely the QCD scale Λ_{QCD}, the transverse momentum scale for space-like parton-shower evolution Q^2_{max}, the h_{damp} parameter [86] and the used P2012 RadLo and RadHi tunes [28]. In Ref. [85] it was shown

that a number of final state distributions are better accounted for by these POWHEG+PYTHIA samples with $h_{\text{damp}} \approx m_{\text{top}}$. Therefore, these samples are used for evaluating this uncertainty, taking half the observed difference between the up variation and the down variation sample. Because the parameterisations for the template fit to data are obtained from POWHEG+PYTHIA samples using $h_{\text{damp}} = \infty$, it was verified that, considering the method uncertainty quoted in Table 3, applying the functions to the $h_{\text{damp}} \approx m_{\text{top}}$ samples leads to a result consistent with the input top mass.

Underlying event (UE): The difference in UE modelling is assessed by comparing POWHEG-BOX samples based on the same partonic events generated with the CT10 PDFs. A sample with the P2012 tune is compared to a sample with the P2012 MPIHI tune [28], with both tunes using the same CTEQ6L1 PDFs [87] for PS and hadronisation. The Perugia 2012 MPIHI tune provides more semi-hard multiple parton interactions and is used for this comparison with identical colour reconnection (CR) parameters in both tunes. The full observed difference is assigned as a systematic uncertainty.

Colour reconnection (CR): This systematic uncertainty is estimated using samples with the same partonic events as for the UE uncertainty evaluation, but with the P2012 tune and the P2012 LOCR tune [28] for PS and hadronisation. The CR effects are estimated by assigning the full difference observed between samples.

Parton distribution function (PDF): The PDF systematic uncertainty is the sum in quadrature of three contributions. These are the sum in quadrature of the differences in m_{top} for the 26 eigenvector variations of the CTEQ PDF [29] and two differences in m_{top} obtained from reweighting the central CT10 PDF set to the MSTW2008 PDF [40] and the NNPDF2.3 PDF [43].

7.3 Modelling of background processes

The mismodelling of the background processes is taken into account by variation of the corresponding normalisations and shapes of the distributions.

Background normalisation: The normalisations are varied for the data-driven background estimates according to their uncertainties. For the negligible contribution of diboson production, no normalisation uncertainty is evaluated.

Background shape: For the W+jets background, the shape uncertainty is evaluated from the variation of the heavy flavour fractions. The corresponding uncertainty is found to be small. Given the very small contribution from Z+jets, diboson and NP/fake-lepton backgrounds, for these background sources no shape uncertainty is evaluated.

7.4 Detector modelling

The limited knowledge of the detector, and of the particle interactions therein, is reflected in numerous systematic uncertainties.

Jet energy scale (JES): Mean jet energies can be measured with a relative precision of about 1% to 4%, typically falling with increasing jet p_{T} and rising with increasing jet $|\eta|$ [88, 89]. The total JES uncertainty consists of more than 60 subcomponents, originating from the various steps in the jet calibration. The number of these nuisance parameters is reduced with a matrix diagonalisation of the full JES covariance matrix, including all nuisance parameters of a given category of the JES uncertainty components.

The analyses of $\sqrt{s}$ = 7 TeV and $\sqrt{s}$ = 8 TeV data make use of the EM+JES and the LCW+GSC [88] jet calibrations, respectively. The two calibrations feature different sets of nuisance parameters, and the LCW+GSC calibration is generally more precise than the EM+JES calibration. While the pile-up correction for the jet calibration for 7 TeV data only depends on the number of primary vertices (n_{vtx}) and the average number of interactions per bunch crossing ($\langle\mu\rangle$), a jet-area based pile-up subtraction method is introduced for the 8 TeV data. Additional terms to account for uncertainties in the pile-up estimation, which depend on the jet p_{T} and the local energy density, and the punch-through uncertainty are added. The final reduced number of nuisance parameters for the 8 TeV analysis is therefore 25. This uncertainty is the dominant systematic uncertainty for all results shown in Table 3. Performing only a one-dimensional fit to $m_{\mathrm{top}}^{\mathrm{reco}}$ or two-dimensional fit to $m_{\mathrm{top}}^{\mathrm{reco}}$ and m_{W}^{reco} would result in a total JES uncertainty of 0.99 GeV or 0.74 GeV, respectively.

Relative *b*-to-light-jet energy scale (bJES): The bJES is an additional uncertainty for the remaining differences between *b*-jets and light jets after the global JES is applied and therefore the corresponding uncertainty is uncorrelated with the JES uncertainty. Jets containing *B*-hadrons are assigned an additional uncertainty of 0.2% to 1.2%, with the lowest uncertainties for high-p_{T} *b*-jets [61]. Due to the determination of bJSF, the bJES uncertainty in Table 3 is a very small contribution to the uncertainty in m_{top}. However, performing only a two-dimensional fit to $m_{\mathrm{top}}^{\mathrm{reco}}$ and m_{W}^{reco} would result in an uncertainty of 0.47 GeV.

Jet energy resolution (JER): The JER is determined following an eigenvector decomposition strategy similar to the JES systematic uncertainties. The components take into account various effects evaluated from MC-to-data comparisons including calorimeters noise terms in the forward region. The JER uncertainty is determined by the sum in quadrature of the components of the eigenvector decomposition.

Jet reconstruction efficiency (JRE): The JRE uncertainty is evaluated by randomly removing 0.23% of the jets with $p_{\mathrm{T}} < 30$ GeV from the MC simulated events prior to the event selection to reflect the precision with which the data-to-MC JRE ratio is known [60]. The fitted m_{top} difference between the varied sample and the nominal sample is taken as a systematic uncertainty.

Jet vertex fraction (JVF): When summing the scalar p_{T} of all tracks in a jet, the JVF is the fraction contributed by tracks originating at the primary vertex. The uncertainty in m_{top} is evaluated by varying the requirement on the JVF within its uncertainty [63].

***b*-tagging:** Mismodelling of the *b*-tagging efficiency and mistag rate is accounted for by the application of jet-specific scale factors to MC simulated events [64]. These scale factors depend on jet p_{T}, jet η, and the underlying quark flavour. The ones used in this analysis are derived from dijet and $t\bar{t} \rightarrow$ dilepton [64] events. Similar to the JES uncertainties, the *b*-tagging uncertainties are estimated by using an eigenvector approach, based on the *b*-tagging calibration analysis [64, 90, 91]. They include the uncertainties in the

b-tagging, c/τ-tagging and mistagging scale factors. Their impact is derived by varying the scale factors within their uncertainties and adding the resulting fitted differences in quadrature. In this procedure, uncertainties that are considered both in the b-tagging calibration and as separate sources in the m_{top} analysis are taken into account in a correlated way by varying the corresponding b-tagging scale factors together with the varied sample used to assess the impact on m_{top}. The final b-tagging uncertainty is the sum in quadrature of these uncorrelated components. Compared to the result on $\sqrt{s} = 7$ TeV data, the b-tagging uncertainty is reduced by about one third, for both the standard and the BDT event selections, likely due to the improvements made in the b-tagging itself. The b-tagging scale factors are the same as those used for the $t\bar{t} \to$ dilepton events in Ref. [14]. Since the b-tagging scale factor determination is systematically limited, the statistical correlation, induced by the use of the scale factors obtained from $t\bar{t} \to$ dilepton events in the same channel they are derived in, is estimated to be negligible.

Leptons: The lepton uncertainties are related to the electron energy or muon momentum scale and resolution, as well as trigger, isolation and identification efficiencies. These are measured very precisely in high purity $J/\psi \to \ell\ell$ and $Z \to \ell\ell$ data [55, 56, 92]. For each component, the corresponding uncertainty is propagated to the analysis by variation of the respective quantity. The changes are propagated to the $E_{\text{T}}^{\text{miss}}$ as well.

Missing transverse momentum ($E_{\text{T}}^{\text{miss}}$): The remaining contribution to the $E_{\text{T}}^{\text{miss}}$ uncertainty stems from the uncertainties in calorimeter cell energies associated with low-p_{T} jets (7 GeV $< p_{\text{T}} <$ 20 GeV), without any corresponding reconstructed physics object, or from pile-up interactions. Their impact is accounted for as described in Ref. [65]. The corresponding uncertainty in m_{top} is small.

Pile-up: Besides the component treated in the JES, the residual dependence of the fitted m_{top} on the amount of pile-up activity and a possible MC mismodelling is determined. Within the statistical uncertainties, the m_{top} dependences as functions of n_{vtx} and $\langle\mu\rangle$ are found to be consistent in data and simulation. The pile-up conditions differ between the $\sqrt{s} = 7$ and 8 TeV data. At $\sqrt{s} = 8$ TeV, the average number of inelastic pp interactions per bunch crossing for the BDT selection is $\langle\mu\rangle = 20.3$ and the mean number of reconstructed primary vertices is about $n_{\text{vtx}} = 9.4$, compared to $\langle\mu\rangle = 8.8$ and $n_{\text{vtx}} = 7.0$ at $\sqrt{s} = 7$ TeV [63]. The corresponding uncertainty is somewhat larger than for $\sqrt{s} = 7$ TeV data, but still small.

7.5 Statistical precision of systematic uncertainties

The systematic uncertainties quoted in Table 3 carry statistical uncertainties themselves. In view of a combination with other measurements, the statistical precision from a comparison of two samples σ is determined for each uncertainty source based on the statistical correlation ρ_{12} of the underlying samples, using $\sigma^2 = \sigma_1^2 + \sigma_2^2 - 2\rho_{12}\sigma_1\sigma_2$. The statistical correlation is expressed as a function of the fraction of shared events of both samples $\rho_{12} = \sqrt{N_{12}/N_1 \cdot N_{12}/N_2} = N_{12}/\sqrt{N_1 \cdot N_2}$, with N_1 and N_2 the unweighted numbers of events in the two samples, and N_{12} the unweighted number of events present in both samples. The size of the MC sample at $m_{\text{top}} = 172.5$ GeV results in a statistical precision in m_{top} of about 100 MeV. Most estimations are based on the same sample with only a change in a single parameter, like lepton energy scale uncertainties. This leads to a high correlation of the central m_{top} values and a correspondingly low statistical uncertainty in their difference. Others, which do not share the same generated events or exhibit

other significant differences, have a lower correlation and the corresponding statistical uncertainty is higher, like in the case of the signal MC modelling uncertainty. The statistical uncertainty of the total systematic uncertainty is calculated from the individual statistical uncertainties by the propagation of uncertainties.

8 Results in the data

The likelihood fit to the data results in

$$\begin{aligned} m_{\text{top}} &= 172.08 \pm 0.39\,(\text{stat})\,\text{GeV}\,, \\ \text{JSF} &= 1.005 \pm 0.001\,(\text{stat})\,, \\ \text{bJSF} &= 1.008 \pm 0.005\,(\text{stat})\,. \end{aligned}$$

The statistical uncertainties are taken from the parabolic approximation of the likelihood profiles. They are properly described by the expected statistical uncertainties calculated above. The correlation of the three variables with $i = 0, 1, 2$ corresponding to m_{top}, JSF and bJSF are:

$$\rho_{\text{stat}} = \begin{pmatrix} 1 & & \\ -0.27 & 1 & \\ -0.92 & -0.02 & 1 \end{pmatrix} \quad \text{and} \quad \rho_{\text{tot}} = \begin{pmatrix} 1 & & \\ -0.30 & 1 & \\ -0.39 & -0.42 & 1 \end{pmatrix}.$$

The left matrix corresponds to the correlations for statistical uncertainties only, while the right matrix is obtained additionally taking into account all systematic uncertainties.

Figure 6 shows the $m_{\text{top}}^{\text{reco}}$, m_W^{reco}, and R_{bq}^{reco} distributions in the data together with the corresponding fitted probability density functions for the background alone (barely visible at the bottom of the figure) and for the sum of signal and background. The uncertainty band attached to the fit to data is obtained in the following way. At each point in $m_{\text{top}}^{\text{reco}}$, m_W^{reco}, and R_{bq}^{reco}, the band contains 68% of all fit function values obtained by randomly varying m_{top}, JSF and bJSF within their total uncertainties and taking into account the corresponding correlations. The waist in the uncertainty band is caused by the usage of normalised probability density functions.

The measured value of m_{top} in the $t\bar{t} \to$ lepton + jets channel at $\sqrt{s} = 8$ TeV is:

$$m_{\text{top}} = 172.08 \pm 0.39\,(\text{stat}) \pm 0.82\,(\text{syst})\,\text{GeV},$$

with a total uncertainty of 0.91 GeV. The statistical precision of the systematic uncertainty is 0.06 GeV. This result corresponds to a 19% improvement with respect to the result obtained using the standard selection on the same data. Compared to the result in the $t\bar{t} \to$ lepton + jets channel at $\sqrt{s} = 7$ TeV, the improvement is 29%. On top of the smaller statistical uncertainty, the increased precision is mainly driven by a lower impact of the theory modelling uncertainties achieved by the BDT selection. The larger number of events in the $\sqrt{s} = 8$ TeV dataset is effectively traded for lower systematic uncertainties, resulting in a significant gain in total precision. The new ATLAS result in the $t\bar{t} \to$ lepton + jets channel is more precise than the result from the CDF experiment, but less precise than the CMS and D0 results, measured in the same channel.

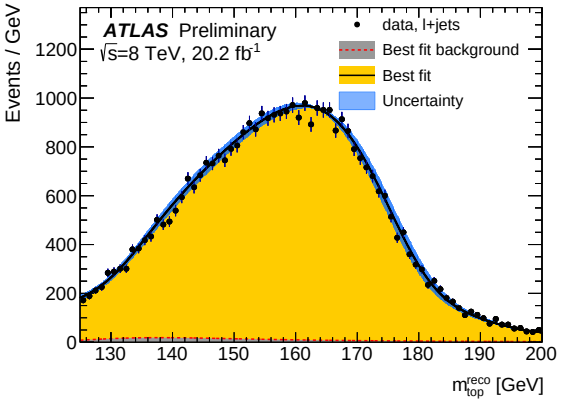

(a) Reconstructed top quark mass

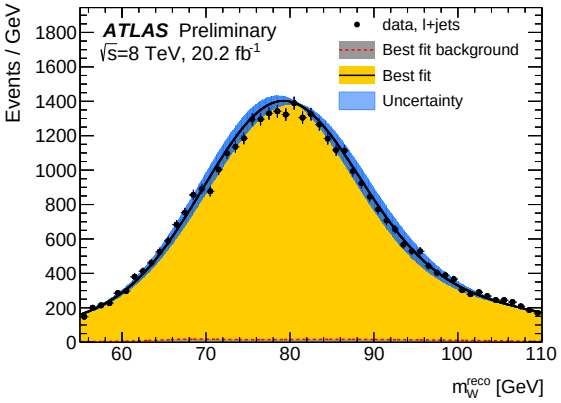

(b) Reconstructed W boson mass

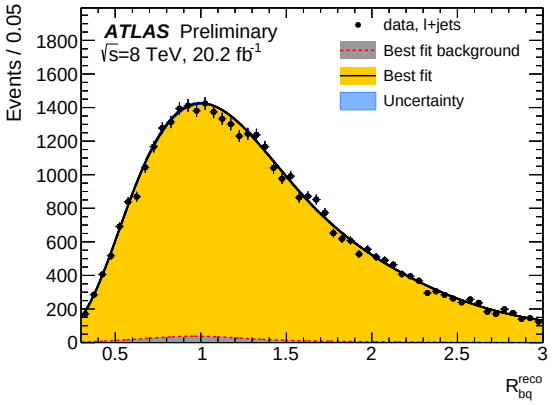

(c) Reconstructed ratio of jet transverse momenta

Figure 6: Results of the likelihood fit to the data. The figures show the data distributions of the three observables with statistical uncertainties together with the fitted probability density function for the background alone (barely visible at the bottom of the figure) and for the sum of signal and background. The uncertainty band corresponds to the one standard deviation total uncertainty on the fit function. It is based on the total uncertainty in the three fitted parameters as explained in the text. Figure (a) shows the distribution of the reconstructed top quark mass $m_{\text{top}}^{\text{reco}}$, figure (b) the distribution of the reconstructed W boson mass m_W^{reco}, and finally figure (c) the distribution of the reconstructed ratio of jet transverse momenta R_{bq}^{reco}.

9 Combination with previous ATLAS measurements

This section presents the combination of the m_{top} results of the ATLAS analyses in the $t\bar{t} \to$ dilepton and $t\bar{t} \to$ lepton + jets channels at centre-of-mass energies of $\sqrt{s} = 7$ and 8 TeV. The combination follows the approach developed for the combination of the $\sqrt{s} = 7$ TeV analyses in Ref. [9], including the evaluation of the correlations. The treatment of uncertainty categories for the two measurements at $\sqrt{s} = 7$ TeV exactly follows Ref. [9]. For the mapping of uncertainty categories for data taken at different centre-of-mass energies, required for the combination with results at $\sqrt{s} = 8$ TeV, the choice of Ref. [14] is taken. The most complex cases are the uncertainty components involving eigenvector decompositions, like the JES and b-tagging scale factor uncertainties, and the uncertainty categories that were added or removed.

The PDF uncertainty components are based on the same variations and PDF sets for the $\sqrt{s} = 7$ and 8 TeV measurements and can therefore trivially be related to each other. The JES induced uncertainty in m_{top} is obtained from a number of JES sub-components. Some JES sub-components have an equivalent at the other centre-of-mass energy, others do not. As in the $t\bar{t} \to$ dilepton analysis Ref. [14], the JES sub-components without an equivalent at the other centre-of-mass energy are treated as independent, resulting in vanishing estimator correlations for that part of the covariance. For the remaining sub-components, the estimator correlations are partly positive and partly negative. The estimator correlations for the dominating flavour uncertainties are negative. Consequently, the resulting estimator correlations for the total JES uncertainty are negative. Different assumptions on the equivalence of the JES components between the datasets at the two centre-of-mass energy lead to a +19 MeV change in the central value and a −1 MeV change in the final uncertainty, which is insignificant compared to the statistical precision of the uncertainty in the combined result given below.

Furthermore, the $\sqrt{s} = 7$ and 8 TeV measurements are treated as uncorrelated for the nuisance parameters of the b-tagging, c/τ-tagging, mistagging and JER uncertainties. In Ref. [14] it was shown that a correlated treatment of the flavour-tagging nuisance parameters results in an insignificant change in the combination. Finally, for the statistical, method calibration, MC-based background shape at $\sqrt{s} = 7$ TeV, and the pile-up uncertainties in m_{top}, the measurements are assumed to be uncorrelated. Details on the evaluation of the correlations for all the systematic uncertainties are discussed below.

The combination is performed using the best linear unbiased estimate (BLUE) method [93, 94] in a C++ implementation described in Ref. [95]. The BLUE method combines measurements based on a linear combination of the inputs. The coefficients (BLUE weights) are determined via the minimisation of the total variance of the combined result. They can be used to construct measures for the importance of a given single measurement in the combination [94]. The central values, the list of uncertainty components and the correlations ρ of the estimators for each uncertainty component have to be provided. For all uncertainties, a Gaussian probability distribution function is assumed. For the uncertainties in m_{top} for which the measurements are correlated, when using $\pm 1\sigma$ variations of a systematic effect, e.g. when changing the bJES by $\pm 1\sigma$, there are two possibilities. When simultaneously applying a variation for a systematic uncertainty, e.g. $+1\sigma$ for the bJES, to a pair of measurements, e.g. the $t\bar{t} \to$ lepton + jets and $t\bar{t} \to$ dilepton measurements at $\sqrt{s} = 8$ TeV, both analyses can result in a larger or smaller m_{top} value than the one obtained for the nominal case (full correlation, $\rho = +1$), or one analysis can result in a larger and the other in a smaller value (full anti-correlation, $\rho = -1$). Consequently, an uncertainty from a source only consisting of a single variation, such as the bJES induced uncertainty or the uncertainty related to the choice of MC generator for signal events, results in a correlation of $\rho = \pm 1$. The estimator correlations for composite uncertainties are evaluated by calculating the correlation from the subcomponents. For any

pair of measurements (1, 2), this is done by adding the covariance terms of the subcomponents k with $\rho_k = \pm 1$ and dividing by the total uncertainties for that source. The resulting correlation:

$$\rho_{12} = \frac{\sum_{k=1}^{N_{\text{comp}}} \rho_k \sigma_{1k} \sigma_{2k}}{\sigma_1 \sigma_2},$$

is quoted in Table 4 and used in the combination. The quantity $\sigma_i^2 = \sum_{k=1}^{N_{\text{comp}}} \sigma_{ik}^2$ with $i = 1, 2$ is the sum of the single subcomponent variances in analysis i. Besides the usual composite components based on eigenvector decomposition like the JES uncertainty, this is also applied to the background normalisation. This procedure is merely applied to reduce the large list of uncertainty components to a reasonable number of uncertainty classes, i.e. to those given in Table 5. Since the total covariance matrix is independent of any chosen subset of partial sums, this does not affect the combination. The evaluated shifts in m_{top} for the various uncertainty subcomponents in pairs of analyses, denoted by $\Delta m_{\text{top}}^{\text{l+jets}}$ and $\Delta m_{\text{top}}^{\text{dil}}$, are shown in Figures 7(a) and 7(b). Each point represents the observed shifts for a systematic uncertainty together with a cross, indicating the corresponding statistical precision of the systematic uncertainty in the $t\bar{t} \to$ lepton + jets and the $t\bar{t} \to$ dilepton channels at the respective centre-of-mass energy. The red full points indicate the fully correlated cases, the blue open points the anti-correlated. For the $t\bar{t} \to$ lepton + jets and $t\bar{t} \to$ dilepton measurements at $\sqrt{s} = 8$ TeV, shown in Figure 7(a), the measurements are anti-correlated for many significant sources of uncertainty. This is caused by the in-situ measurement of the jet energy scale factor (JSF) and relative b-to-light-jet energy scale factor (bJSF) in the three-dimensional $t\bar{t} \to$ lepton + jets analysis. A similar pattern is observed for the $t\bar{t} \to$ lepton + jets measurements at the two centre-of-mass energies, shown in Figure 7(b).

The central values of the four individual measurements, their uncertainty components, and the estimated correlations between the three previous measurements and the new result in the $t\bar{t} \to$ lepton + jets channel for all sources of uncertainty, are given in Table 4. For each result, the evaluated systematic uncertainties are shown followed by their statistical uncertainties. These statistical uncertainties are propagated to the statistical uncertainties of the total systematic uncertainties and the total uncertainties[6]. The dependences of the combined central values and total uncertainties on the total correlation of the combination of the $t\bar{t} \to$ lepton + jets and $t\bar{t} \to$ dilepton measurements at $\sqrt{s} = 8$ TeV are shown in Figures 7(c) and 7(d).

Based on Table 4 and the correlations of the previous measurements for all sources of systematic uncertainties given in Ref. [14], selected combinations are performed. The corresponding results are given in Table 5. The correlations of the measurements and their BLUE weights for the new ATLAS combination are given in Table 6. The measurements at $\sqrt{s} = 8$ TeV are significantly more precise and also less correlated than those at $\sqrt{s} = 7$ TeV. Consequently, the size of the uncertainty of the combined result at $\sqrt{s} = 8$ TeV ($m_{\text{top}}^{\text{8TeV}}$) is 38% smaller than the one obtained from the measurements at $\sqrt{s} = 7$ TeV ($m_{\text{top}}^{\text{7TeV}}$).

Treating the measurements in the two $t\bar{t}$ decay channels as determining different masses, namely $m_{\text{top}}^{\text{l+jets}}$ and $m_{\text{top}}^{\text{dil}}$, results in consistent values, i.e. the data do not show any sign of a decay-channel-dependent m_{top}. The correlation of $m_{\text{top}}^{\text{l+jets}}$ and $m_{\text{top}}^{\text{dil}}$ is -0.15 and the χ^2 probability for determining the same m_{top} is $P(\chi^2, 1) = 51\%$. Given that no dependence of m_{top} on the centre-of-mass energy or the W decay channel is expected, the above examples of combinations are merely investigations for the consistency of the input measurements. Finally, the distribution of the compatibilities of all pairs of measurements is investigated.

[6] For the previous results, the values quoted differ from the ones in the original publications, where the sum in quadrature of the statistical uncertainties of the individual systematic uncertainties was used.

	$\sqrt{s}$ = 7 TeV		$\sqrt{s}$ = 8 TeV		Correlations		
	$m_{\text{top}}^{\text{dil}}$ [GeV]	$m_{\text{top}}^{\text{l+jets}}$ [GeV]	$m_{\text{top}}^{\text{dil}}$ [GeV]	$m_{\text{top}}^{\text{l+jets}}$ [GeV]	ρ_{03}	ρ_{13}	ρ_{23}
Results	173.79	172.33	172.99	172.08			
Statistics	0.54	0.75	0.41	0.39	0	0	0
– *Stat. comp.* (m_{top})		0.23		0.11			
– *Stat. comp.* (JSF)		0.25		0.11			
– *Stat. comp.* (bJSF)		0.67		0.35			
Method	0.09 ± 0.07	0.11 ± 0.10	0.05 ± 0.07	0.13 ± 0.11	0	0	0
Signal Monte Carlo generator	0.26 ± 0.16	0.22 ± 0.21	0.09 ± 0.15	0.16 ± 0.17	+1.00	+1.00	+1.00
Hadronisation	0.53 ± 0.09	0.18 ± 0.12	0.22 ± 0.09	0.15 ± 0.10	−1.00	−1.00	−1.00
Initial- and final-state QCD radiation	0.47 ± 0.05	0.32 ± 0.06	0.23 ± 0.07	0.08 ± 0.11	+1.00	−1.00	+1.00
Underlying event	0.05 ± 0.05	0.15 ± 0.07	0.10 ± 0.14	0.08 ± 0.15	+1.00	−1.00	+1.00
Colour reconnection	0.14 ± 0.05	0.11 ± 0.07	0.03 ± 0.14	0.19 ± 0.15	−1.00	+1.00	−1.00
Parton distribution function	0.11 ± 0.00	0.25 ± 0.00	0.05 ± 0.00	0.09 ± 0.00	+0.72	+0.72	−0.48
Background normalisation	0.04 ± 0.00	0.10 ± 0.00	0.03 ± 0.00	0.08 ± 0.00	−0.77	−0.74	−0.06
W/Z+jets shape	0.00 ± 0.00	0.29 ± 0.00	0	0.11 ± 0.00	0	0	0
Fake leptons shape	0.01 ± 0.00	0.05 ± 0.00	0.07 ± 0.00	0	0	0	0
Jet energy scale	0.75 ± 0.08	0.58 ± 0.11	0.54 ± 0.04	0.54 ± 0.02	+0.18	−0.29	−0.54
Relative b-to-light-jet energy scale	0.68 ± 0.02	0.06 ± 0.03	0.30 ± 0.01	0.03 ± 0.01	+1.00	+1.00	+1.00
Jet energy resolution	0.19 ± 0.04	0.22 ± 0.11	0.09 ± 0.05	0.20 ± 0.04	0	0	+0.22
Jet reconstruction efficiency	0.07 ± 0.00	0.12 ± 0.00	0.01 ± 0.00	0.02 ± 0.01	+1.00	+1.00	+1.00
Jet vertex fraction	0.00 ± 0.00	0.01 ± 0.00	0.02 ± 0.00	0.09 ± 0.01	−1.00	+1.00	+1.00
b-tagging	0.07 ± 0.00	0.50 ± 0.00	0.04 ± 0.02	0.38 ± 0.00	0	0	−0.23
Leptons	0.13 ± 0.00	0.04 ± 0.00	0.14 ± 0.01	0.16 ± 0.01	−0.08	−0.17	+0.11
$E_{\text{T}}^{\text{miss}}$	0.04 ± 0.03	0.15 ± 0.04	0.01 ± 0.01	0.05 ± 0.01	−0.12	+0.22	+0.97
Pile-up	0.01 ± 0.00	0.02 ± 0.01	0.05 ± 0.01	0.15 ± 0.01	0	0	0
Total systematic uncertainty	1.31 ± 0.07	1.03 ± 0.08	0.74 ± 0.05	0.82 ± 0.06			
Total	1.41 ± 0.07	1.27 ± 0.08	0.85 ± 0.05	0.91 ± 0.06	0.06	−0.07	−0.19

Table 4: The four measured values of m_{top} and their statistical and systematic uncertainty components are shown on the left. The right part reports the pairwise correlations ρ_{i3} of the previous measurements with the $t\bar{t} \to$ lepton + jets measurement at $\sqrt{s}$ = 8 TeV. The indices are 0 = $t\bar{t} \to$ dilepton at $\sqrt{s}$ = 7 TeV, 1 = $t\bar{t} \to$ lepton + jets at $\sqrt{s}$ = 7 TeV, both from Ref. [9], 2 = $t\bar{t} \to$ dilepton at $\sqrt{s}$ = 8 TeV from Ref. [14] and 3 = $t\bar{t} \to$ lepton + jets at $\sqrt{s}$ = 8 TeV. The pairwise correlations of the previous measurements can be found in Ref. [14]. For the individual measurements, the systematic uncertainty in m_{top} and its associated statistical uncertainty is given for each source of uncertainty. Assigned correlations are given as integer values, determined correlations are shown as real values. The last line refers to the sum in quadrature of the statistical and systematic uncertainty components or the total correlations, respectively. The statistical uncertainty in the total systematic uncertainties and in the total uncertainties are calculated from the propagation of uncertainties.

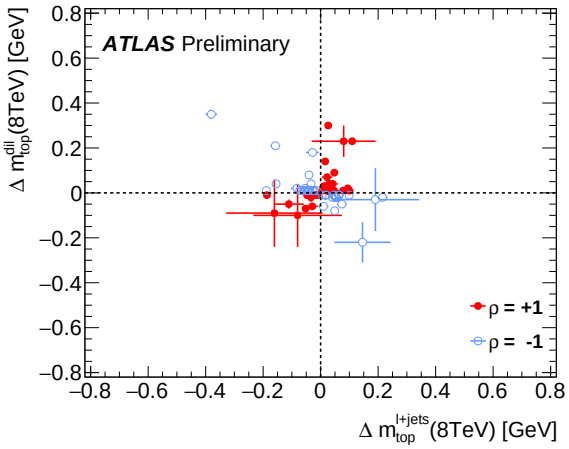

(a) $t\bar{t} \to$ lepton + jets (8 TeV) and $t\bar{t} \to$ dilepton (8 TeV)

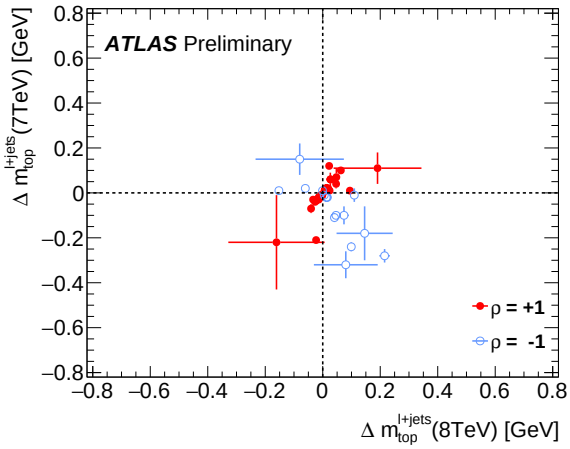

(b) $t\bar{t} \to$ lepton + jets (8 TeV) and $t\bar{t} \to$ lepton + jets (7 TeV)

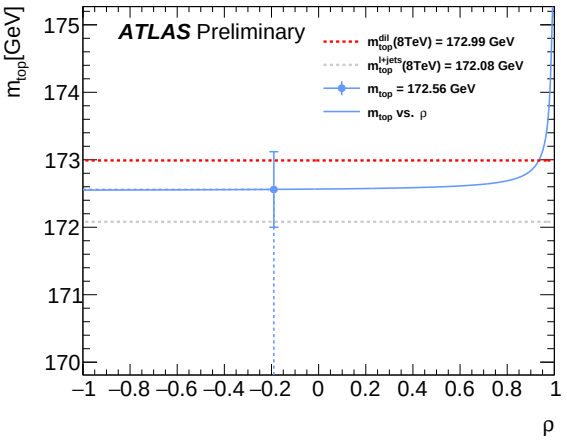

(c) $t\bar{t} \to$ lepton + jets (8 TeV) and $t\bar{t} \to$ dilepton (8 TeV)

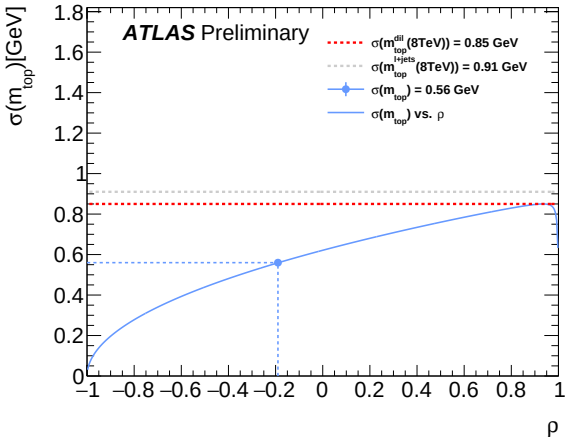

(d) $t\bar{t} \to$ lepton + jets (8 TeV) and $t\bar{t} \to$ dilepton (8 TeV)

Figure 7: The pairwise differences in m_{top} when simultaneously varying a pair of measurements for the subcomponents of a systematic uncertainty and the combination of the two results from $\sqrt{s}$ = 8 TeV data. Figure (a) shows the correlations of the present measurement with the result in the $t\bar{t} \to$ dilepton channel at $\sqrt{s}$ = 8 TeV, and figure (b) those to the result in the $t\bar{t} \to$ lepton + jets channel at $\sqrt{s}$ = 7 TeV. The sizes of the crosses indicate the statistical precisions of the systematic uncertainties. The red full points indicate the fully correlated cases, the blue open points the anti-correlated ones. Figure (c) shows the combined value and figure (d) the uncertainty of the combination of the two results from $\sqrt{s}$ = 8 TeV data as functions of their correlation (blue full line). The blue point corresponds to the actual correlation. For comparison, the corresponding values for the input measurements are also shown (grey and red dashed lines).

	Consistency evaluation				**Measurement**
	$m_{\text{top}}^{7\text{TeV}}$ [GeV]	$m_{\text{top}}^{8\text{TeV}}$ [GeV]	$m_{\text{top}}^{\text{l+jets}}$ [GeV]	$m_{\text{top}}^{\text{dil}}$ [GeV]	m_{top} [GeV]
Results	172.99	172.56	172.11	173.02	172.51
Statistics	0.48	0.28	0.36	0.39	0.27
Method	0.07	0.07	0.09	0.05	0.06
Signal Monte Carlo generator	0.24	0.12	0.17	0.10	0.14
Hadronisation	0.34	0.05	0.06	0.22	0.07
Initial- and final-state QCD radiation	0.04	0.16	0.07	0.26	0.07
Underlying event	0.06	0.09	0.01	0.11	0.05
Colour reconnection	0.01	0.07	0.17	0.03	0.08
Parton distribution function	0.17	0.04	0.13	0.05	0.07
Background normalisation	0.07	0.04	0.04	0.03	0.03
W/Z+jets shape	0.16	0.05	0.12	0.01	0.07
Fake leptons shape	0.03	0.04	0.02	0.07	0.03
Jet energy scale	0.41	0.26	0.33	0.52	0.21
Relative b-to-light-jet energy scale	0.34	0.17	0.01	0.32	0.15
Jet energy resolution	0.03	0.11	0.16	0.09	0.10
Jet reconstruction efficiency	0.10	0.02	0.05	0.01	0.03
Jet vertex fraction	0.00	0.06	0.07	0.02	0.05
b-tagging	0.25	0.18	0.31	0.04	0.17
Leptons	0.05	0.11	0.11	0.14	0.09
$E_{\text{T}}^{\text{miss}}$	0.08	0.03	0.07	0.01	0.04
Pile-up	0.01	0.08	0.10	0.05	0.06
Total systematic uncertainty	0.77	0.48	0.61	0.74	0.42
Total	0.91	0.56	0.71	0.84	0.50

Table 5: The results for selected combinations based on the measurements at $\sqrt{s} = 7$ and 8 TeV. The left two columns show the combination of the two measurements at $\sqrt{s} = 7$ TeV ($m_{\text{top}}^{7\text{TeV}}$) from Ref. [9] and the combination of the two measurements at $\sqrt{s} = 8$ TeV ($m_{\text{top}}^{8\text{TeV}}$), both combinations neglecting the results at the respective other centre-of-mass energy. The two middle columns show the combination of the four measurements ($m_{\text{top}}^{\text{l+jets}}$, $m_{\text{top}}^{\text{dil}}$) assuming pairs of measurements to determine a decay-specific top quark mass, namely $m_{\text{top}}^{\text{l+jets}}$ and $m_{\text{top}}^{\text{dil}}$. Finally, the new ATLAS result in m_{top} is shown on the right. It is obtained from combining the two measurements at $\sqrt{s} = 8$ TeV and the measurement in the $t\bar{t} \to$ lepton + jets channel at $\sqrt{s} = 7$ TeV. For each combination, the systematic uncertainty is given for each source of uncertainty. The last line refers to the sum in quadrature of the statistical and systematic uncertainty components.

Correlations	$m_{\text{top}}^{\text{dil}}$ (7 TeV)	$m_{\text{top}}^{\text{l+jets}}$ (7 TeV)	$m_{\text{top}}^{\text{dil}}$ (8 TeV)	$m_{\text{top}}^{\text{l+jets}}$ (8 TeV)
$m_{\text{top}}^{\text{dil}}$ (7 TeV)	1.00			
$m_{\text{top}}^{\text{l+jets}}$ (7 TeV)	−0.07	1.00		
$m_{\text{top}}^{\text{dil}}$ (8 TeV)	0.52	0.00	1.00	
$m_{\text{top}}^{\text{l+jets}}$ (8 TeV)	0.06	−0.07	−0.19	1.00
BLUE weight (m_{top})	-	0.17	0.43	0.40

Table 6: Pairwise correlations of the individual measurements and BLUE weights for the chosen combination. The upper part reports the correlations of the four measurements of m_{top}. The lower part lists the BLUE weights for the combination of m_{top} listed in Table 5.

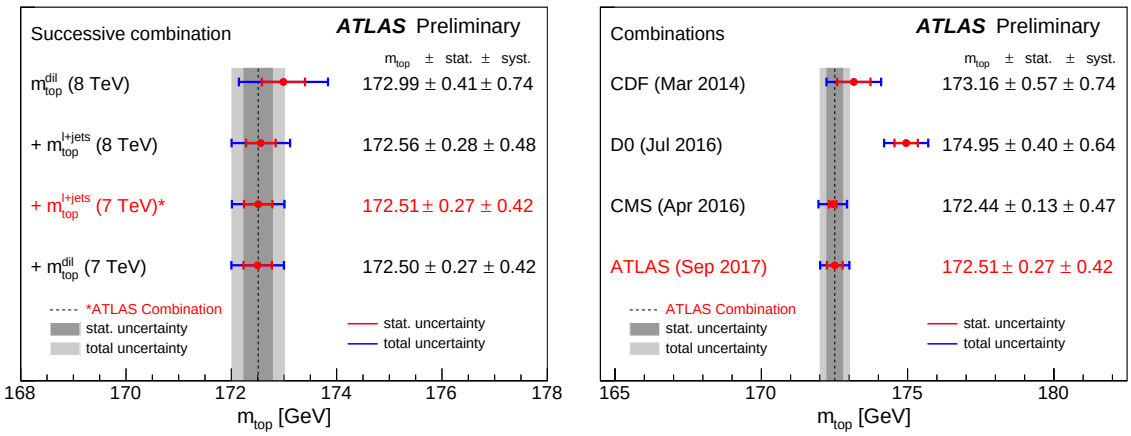

(a) Successive combination

(b) Combinations

Figure 8: Results of the combination. Figure (a) shows the combined result when successively adding results to the most precise one. Each line of this figure shows the combined result, when adding the result listed to the combination, indicated by a '+'. The new ATLAS combination is shown in red and indicated by the star. Figure (b) shows the combined result for m_{top} per experiment from the latest combinations performed by the individual experiments. In this figure the vertical band corresponds to the present ATLAS combination of m_{top}. For CDF, the statistical component caused by the in-situ determination of the jet scale factor is included in the systematic uncertainty.

For each pair of measurements, their compatibility is expressed by the squared ratio of the difference of the pair of measurements divided by the uncertainty in this difference. The distribution of the compatibilities reveals good compatibilities of all measurements, with the smallest χ^2 probability being $P(\chi^2, 1) = 30\%$.

The use of the statistical uncertainties in the systematic uncertainties has two main advantages. Firstly, it allows for properly determining the uncertainties in the evaluation of the total correlations of the estimators, limiting the need of performing ad-hoc variations. Secondly, it enables the combination to be performed, while restricting the combined result to the use of the significant measurements. The significance of the individual measurements in the combination is visualised in Figure 8(a). In this figure, starting from the most precise result, i.e. the $t\bar{t} \rightarrow$ dilepton measurement at $\sqrt{s} = 8$ TeV, with a statistical precision in the total uncertainty of 0.05 GeV, measurements are added to the combination one at a time according to their importance, and the combined result is reported. Each line of this figure shows the combined result when

adding this result to the input of the combination, indicated by the '+' in front of the name of the added estimator. A detailed discussion of this concept is given in Ref. [94].

Given the statistical precision in the uncertainty of the most precise result, the inclusion of the $t\bar{t} \rightarrow$ lepton + jets measurement at $\sqrt{s} = 8$ TeV significantly improves the combination, leading to the result quoted, which has a reduced statistical uncertainty of the total uncertainty compared to the one of the most precise result. The same is found when adding the $t\bar{t} \rightarrow$ lepton + jets measurement at $\sqrt{s} = 7$ TeV, while using the statistical uncertainty in the previous combination. In contrast, the combination including the 7 TeV $t\bar{t} \rightarrow$ dilepton measurement, which is shown below the one quoted in red in Figure 8(a), does not improve the result. This is a consequence of the estimator properties, i.e. of the uncertainties and correlations of the various ways to measure m_{top} using these analyses, and particularly, it is independent of the actual individual values of m_{top} measured by the estimators. Adding the $t\bar{t} \rightarrow$ dilepton measurement at $\sqrt{s} = 7$ TeV results in an insignificant change compared to the statistical precision in the uncertainty of the previous combined result. Nevertheless, this measurement contains useful information since it provides a partially independent measurement of the top quark mass that leads to a compatible value.

The impact of variations of the input systematic uncertainties within their statistical uncertainties on the central value and the combined total uncertainty is investigated. The distributions are obtained from 500 combinations. For each combination, the size of the uncertainty as well as the correlation are newly evaluated, based on random variations of each systematic uncertainty within the corresponding statistical precision. The distributions are very narrow with root-mean-square values of 0.03 GeV for the central value and 0.04 GeV for the combined total uncertainty. This means that the total uncertainty in the combined result quoted is only known with this statistical precision, which, given the size of the total uncertainty, is fully adequate.

The full breakdown of uncertainties for the new combined ATLAS result on m_{top} is reported in the last column of Table 5. The combined result is:

$$m_{\text{top}} = 172.51 \pm 0.27\,(\text{stat}) \pm 0.42\,(\text{syst})\ \text{GeV} = 172.51 \pm 0.50\ \text{GeV}\,.$$

The χ^2 probability of the combination is 78%. This combination provides a 41% improvement with respect to the most precise single input measurement, which is the $t\bar{t} \rightarrow$ dilepton analysis at $\sqrt{s} = 8$ TeV, and improves upon the combined ATLAS result in Ref. [14]. When the combination is repeated replacing the result from the $\sqrt{s} = 8$ TeV data using the BDT selection by the result using the standard selection (see Table 3), the correlation of the $\sqrt{s} = 8$ TeV $t\bar{t} \rightarrow$ lepton + jets result to the $\sqrt{s} = 8$ TeV $t\bar{t} \rightarrow$ dilepton result increases from -0.19 to -0.02, and the total uncertainty is 0.59, which is 18% less precise than the new ATLAS combination with the result from the BDT selection.

In Figure 8(b) the result of the ATLAS combination is compared to the results of the combinations from other experiments. The resulting combined values of m_{top} from the two LHC experiments are close and have similar total uncertainties. The combinations from the Tevatron experiments result in larger uncertainties in m_{top}. The CDF result for m_{top} agrees well with the new ATLAS result, while the D0 result is somewhat larger. The combinations of the various experiments depend on different numbers of input measurements, and achieve significantly different gains in precision over the one without any combination, i.e. over the precision of the respective most precise input result. By far the largest gain is achieved by the ATLAS combination, even though this combination is based on the smallest number of input measurements. This is mostly due to the ATLAS input measurements to the combination being much less correlated with one another than is the case for the respective input measurements to the combinations from the other experiments [10, 12, 13].

10 Conclusion

The top quark mass is measured via a three-dimensional template method in the $t\bar{t} \to$ lepton + jets channel and combined with previous ATLAS m_{top} measurements.

For the $t\bar{t} \to$ lepton + jets analysis at $\sqrt{s} = 8$ TeV, the standard event selection from Ref. [9] is refined. An optimisation employing a BDT selection to efficiently suppress badly reconstructed events results in a significant reduction in total uncertainty, driven by a significant improvement in theory modelling uncertainties. With this approach, the measured value of m_{top} is:

$$m_{\text{top}} = 172.08 \pm 0.39\,(\text{stat}) \pm 0.82\,(\text{syst})\ \text{GeV},$$

with a total uncertainty of 0.91 ± 0.06 GeV, where the quoted uncertainty in the total uncertainty is statistical. The precision is limited by systematic uncertainties, mostly by the calibration of the jet energy scale, b-tagging and by the Monte Carlo modelling of signal events.

The correlations of the measurements are evaluated for all sources of the systematic uncertainty. Using a dedicated mapping of uncertainty categories, a combination with previous ATLAS measurements is performed. Exploiting the statistical uncertainties of the systematic uncertainties to select the input results for the combination, the above measurement in the $t\bar{t} \to$ lepton + jets channel from 8 TeV is combined with the previous ATLAS measurements from 8 TeV data in the $t\bar{t} \to$ dilepton channel and from $\sqrt{s} = 7$ TeV data in the $t\bar{t} \to$ lepton + jets channel, resulting in:

$$m_{\text{top}} = 172.51 \pm 0.27\,(\text{stat}) \pm 0.42\,(\text{syst})\ \text{GeV} = 172.51 \pm 0.50\ \text{GeV},$$

with a total uncertainty of 0.50 ± 0.04 GeV, where the quoted uncertainty in the total uncertainty is statistical. The relative precision of this combination is 0.29%. With this precision in m_{top} achieved, the precise knowledge of the relation between the mass definition of the experimental analysis and the pole mass is becoming relevant. The combined result is mostly limited by the calibration of the jet energy scales and by the Monte Carlo modelling of signal events. This result improves upon the combined ATLAS result in Ref. [14].

References

[1] ALEPH, CDF, D0, DELPHI, L3, OPAL, SLD Collaborations, the LEP Electroweak Working Group, the Tevatron Electroweak Working Group and the SLD Electroweak and Heavy Flavour Groups, *Precision electroweak measurements and constraints on the Standard Model*, (2010), arXiv: 1012.2367 [hep-ex].

[2] M. Baak et al., *The global electroweak fit at NNLO and prospects for the LHC and ILC*, Eur. Phys. J. C **74** (2014) 3046, arXiv: 1407.3792.

[3] Particle Data Group, *Review of Particle Physics*, Chin. Phys. C **38** (2014) 090001.

[4] G. Degrassi et al., *Higgs mass and vacuum stability in the Standard Model at NNLO*, JHEP **8**, 98 (2012) 98, arXiv: 1205.6497 [hep-ph].

[5] F. Bezrukov et al., *The Standard Model Higgs boson as the inflaton*, Phys. Lett. B **659** (2008) 703, arXiv: 0710.3755 [hep-th].

[6] A. De Simone et al., *Running Inflation in the Standard Model*, Phys. Lett. B **678** (2009) 1, arXiv: 0812.4946 [hep-ph].

[7] CDF Collaboration, T. Aaltonen et al., *Precision Top-Quark Mass Measurement at CDF*, Phys. Rev. Lett. **109** (2012) 152003, arXiv: 1207.6758 [hep-ex].

[8] DØ Collaboration, V.M. Abazov et al., *Precision Measurement of the Top Quark Mass in Lepton+Jets Final States*, Phys. Rev. Lett. **113** (2014) 032002, arXiv: 1405.1756 [hep-ex].

[9] ATLAS Collaboration, *Measurement of the top quark mass in the $t\bar{t} \to$ lepton+jets and $t\bar{t} \to$ dilepton channels using $\sqrt{s} = 7$ TeV ATLAS data*, Eur. Phys. J. C **75** (2015) 330, arXiv: 1503.05427 [hep-ex].

[10] CMS Collaboration, *Measurement of the top quark mass using proton-proton data at $\sqrt{(s)} = 7$ and 8 TeV*, Phys. Rev. D **93** (2016) 072004, arXiv: 1509.04044 [hep-ex].

[11] ATLAS, CDF, CMS and D0 Collaborations, *First combination of Tevatron and LHC measurements of the top-quark mass*, (2014), arXiv: 1403.4427 [hep-ex].

[12] CDF Collaboration, T. Aaltonen et al., *Final combination of the CDF results on top-quark mass*, CDF note **11080** (2014), URL: https://www-cdf.fnal.gov/physics/new/top/2014/CDFTopCombo.

[13] D0 Collaboration, V.M. Abazov et al., *Combination of D0 measurements of the top quark mass*, Phys. Rev. D **95** (2017) 112004, arXiv: 1703.06994 [hep-ex].

[14] ATLAS Collaboration, *Measurement of the top quark mass in the $t\bar{t} \to$ dilepton channel from $\sqrt{s} = 8$ TeV ATLAS data*, Phys. Lett. B **761** (2016) 350, arXiv: 1606.02179 [hep-ex].

[15] A. Buckley et al., *General-purpose event generators for LHC physics*, Phys. Rept. **504** (2011) 145, arXiv: 1101.2599 [hep-ph].

[16] S. Moch et al., *High precision fundamental constants at the TeV scale*, (2014), arXiv: 1405.4781 [hep-ph].

[17] M. Butenschoen et al., *Top Quark Mass Calibration for Monte Carlo Event Generators*, Phys. Rev. Lett. **117** (2016) 232001, arXiv: 1608.01318 [hep-ph].

[18] ATLAS Collaboration, *The ATLAS Experiment at the CERN Large Hadron Collider*, JINST **3** (2008) S08003.

[19] ATLAS Collaboration, *Luminosity determination in pp collisions at $\sqrt{s}$ = 8 TeV using the ATLAS detector at the LHC*, Eur. Phys. J. C **76** (2016) 653, arXiv: 1608.03953 [hep-ex].

[20] P. Nason, *A New method for combining NLO QCD with shower Monte Carlo algorithms*, JHEP **11** (2004) 040, arXiv: hep-ph/0409146 [hep-ph].

[21] S. Frixione, P. Nason and C. Oleari, *Matching NLO QCD computations with Parton Shower simulations: the POWHEG method*, JHEP **11** (2007) 070, arXiv: 0709.2092 [hep-ph].

[22] S. Alioli, P. Nason, C. Oleari and E. Re, *A general framework for implementing NLO calculations in shower Monte Carlo programs: the POWHEG BOX*, JHEP **06** (2010) 043, arXiv: 1002.2581 [hep-ph].

[23] S. Frixione, P. Nason and G. Ridolfi, *A Positive-weight next-to-leading-order Monte Carlo for heavy flavour hadroproduction*, JHEP **09** (2007) 126, arXiv: 0707.3088 [hep-ph].

[24] S. Alioli, P. Nason, C. Oleari and E. Re, *NLO single-top production matched with shower in POWHEG: s- and t-channel contributions*, JHEP **09** (2009) 111, arXiv: 0907.4076 [hep-ph], Erratum: JHEP **02** (2010) 011.

[25] E. Re, *Single-top Wt-channel production matched with parton showers using the POWHEG method*, Eur. Phys. J. C **71** (2011) 1547, arXiv: 1009.2450 [hep-ph].

[26] H.-L. Lai et al., *New parton distributions for collider physics*, Phys. Rev. D **82** (2010) 074024, arXiv: 1007.2241 [hep-ph].

[27] T. Sjostrand, S. Mrenna and P. Z. Skands, *PYTHIA 6.4 Physics and Manual*, JHEP **05** (2006) 026, arXiv: hep-ph/0603175 [hep-ph].

[28] P. Z. Skands, *Tuning Monte Carlo Generators: The Perugia Tunes*, Phys. Rev. D **82** (2010) 74018, Consult the E-print version for updates, arXiv: 1005.3457 [hep-ph].

[29] J. Pumplin et al., *New generation of parton distributions with uncertainties from global QCD analysis*, JHEP **07** (2002) 012, arXiv: hep-ph/0201195 [hep-ph].

[30] M. Cacciari, M. Czakon, M. Mangano, A. Mitov and P. Nason, *Top-pair production at hadron colliders with next-to-next-to-leading logarithmic soft-gluon resummation*, Phys. Lett. B **710** (2012) 612, arXiv: 1111.5869 [hep-ph].

[31] P. Bärnreuther, M. Czakon and A. Mitov, *Percent Level Precision Physics at the Tevatron: First Genuine NNLO QCD Corrections to $q\bar{q} \to t\bar{t} + X$*, Phys. Rev. Lett. **109** (2012) 132001, arXiv: 1204.5201 [hep-ph].

[32] M. Czakon and A. Mitov, *NNLO corrections to top-pair production at hadron colliders: the all-fermionic scattering channels*, JHEP **12** (2012) 054, arXiv: 1207.0236 [hep-ph].

[33] M. Czakon and A. Mitov,
NNLO corrections to top pair production at hadron colliders: the quark-gluon reaction,
JHEP **01** (2013) 080, arXiv: 1210.6832 [hep-ph].

[34] M. Czakon, P. Fiedler and A. Mitov,
The total top-quark pair production cross-section at hadron colliders through $O(\alpha_S^4)$,
Phys. Rev. Lett. **110** (2013) 252004, arXiv: 1303.6254 [hep-ph].

[35] M. Czakon and A. Mitov,
Top++: A Program for the Calculation of the Top-Pair Cross-Section at Hadron Colliders,
Comput. Phys. Commun. **185** (2014) 2930, arXiv: 1112.5675 [hep-ph].

[36] N. Kidonakis, *Next-to-next-to-leading-order collinear and soft gluon corrections for t-channel single top quark production*, Phys. Rev. D **83** (2011) 091503, arXiv: 1103.2792 [hep-ph].

[37] N. Kidonakis,
Two-loop soft anomalous dimensions for single top quark associated production with a W- or H-,
Phys. Rev. D **82** (2010) 054018, arXiv: 1005.4451 [hep-ph].

[38] N. Kidonakis, *NNLL resummation for s-channel single top quark production*,
Phys. Rev. D **81** (2010) 054028, arXiv: 1001.5034 [hep-ph].

[39] M. Botje et al., *The PDF4LHC Working Group Interim Recommendations*, (2011),
arXiv: 1101.0538 [hep-ph].

[40] A. D. Martin, W. J. Stirling, R. S. Thorne and G. Watt, *Parton distributions for the LHC*,
Eur. Phys. J. C **63** (2009) 189, arXiv: 0901.0002 [hep-ph].

[41] A. D. Martin, W. J. Stirling, R. S. Thorne and G. Watt, *Uncertainties on alpha(S) in global PDF analyses and implications for predicted hadronic cross sections*, Eur. Phys. J. C **64** (2009) 653,
arXiv: 0905.3531 [hep-ph].

[42] J. Gao et al., *CT10 next-to-next-to-leading order global analysis of QCD*,
Phys. Rev. D **89** (2014) 033009, arXiv: 1302.6246 [hep-ph].

[43] R. D. Ball et al., *Parton distributions with LHC data*, Nucl. Phys. B **867** (2013) 244,
arXiv: 1207.1303 [hep-ph].

[44] M. L. Mangano, M. Moretti, F. Piccinini, R. Pittau and A. D. Polosa,
ALPGEN, a generator for hard multiparton processes in hadronic collisions, JHEP **07** (2003) 001,
arXiv: hep-ph/0206293 [hep-ph].

[45] ATLAS Collaboration, *New ATLAS event generator tunes to 2010 data*, (2011),
URL: http://cds.cern.ch/record/1345343.

[46] K. Melnikov and F. Petriello,
*Electroweak gauge boson production at hadron colliders through O(alpha(s)**2)*,
Phys. Rev. D **74** (2006) 114017, arXiv: hep-ph/0609070 [hep-ph].

[47] G. Corcella, I. Knowles, G. Marchesini, S. Moretti, K. Odagiri et al.,
HERWIG 6: An Event generator for hadron emission reactions with interfering gluons (including supersymmetric processes), JHEP **01** (2001) 010, arXiv: hep-ph/0011363 [hep-ph].

[48] J. M. Butterworth, J. R. Forshaw and M. H. Seymour,
Multiparton interactions in photoproduction at HERA, Z. Phys. C **72** (1996) 637,
arXiv: hep-ph/9601371 [hep-ph].

[49] J. M. Campbell and R. K. Ellis, *An Update on vector boson pair production at hadron colliders*, Phys. Rev. D **60** (1999) 113006, arXiv: hep-ph/9905386 [hep-ph].

[50] T. Sjostrand, S. Mrenna and P. Z. Skands, *A Brief Introduction to PYTHIA 8.1*, Comput. Phys. Commun. **178** (2008) 852, arXiv: 0710.3820 [hep-ph].

[51] ATLAS Collaboration, *Summary of ATLAS PYTHIA 8 tunes*, ATL-PHYS-PUB-2012-003, 2012, URL: http://cdsweb.cern.ch/record/1474107.

[52] ATLAS Collaboration, *The ATLAS Simulation Infrastructure*, Eur. Phys. J. C **70** (2010) 823, arXiv: 1005.4568 [hep-ex].

[53] S. Agostinelli et al., *GEANT4: A simulation toolkit*, Nucl. Instr. Meth. A **506** (2003) 250.

[54] ATLAS Collaboration, *The simulation principle and performance of the ATLAS fast calorimeter simulation FastCaloSim*, (2010), URL: https://cds.cern.ch/record/1300517.

[55] ATLAS Collaboration, *Electron reconstruction and identification efficiency measurements with the ATLAS detector using the 2011 LHC proton–proton collision data*, Eur. Phys. J. C **74** (2014) 2941, arXiv: 1404.2240 [hep-ex].

[56] ATLAS Collaboration, *Measurement of the muon reconstruction performance of the ATLAS detector using 2011 and 2012 LHC proton–proton collision data*, Eur. Phys. J. C **74** (2014) 3130, arXiv: 1407.3935 [hep-ex].

[57] K. Rehermann and B. Tweedie, *Efficient Identification of Boosted Semileptonic Top Quarks at the LHC*, JHEP **03** (2011) 059, arXiv: 1007.2221 [hep-ph].

[58] ATLAS Collaboration, *Topological cell clustering in the ATLAS calorimeters and its performance in LHC Run 1*, (2016), arXiv: 1603.02934 [hep-ex].

[59] M. Cacciari, G. P. Salam and G. Soyez, *The Anti-k(t) jet clustering algorithm*, JHEP **04** (2008) 063, arXiv: 0802.1189 [hep-ph].

[60] ATLAS Collaboration, *Jet energy measurement with the ATLAS detector in proton–proton collisions at* $\sqrt{s} = 7$ *TeV*, Eur. Phys. J. C **73** (2013) 2304, arXiv: 1112.6426 [hep-ex].

[61] ATLAS Collaboration, *Jet energy measurement and its systematic uncertainty in proton–proton collisions at* $\sqrt{s} = 7$ *TeV with the ATLAS detector*, Eur. Phys. J. C **75** (2015) 17, arXiv: 1406.0076 [hep-ex].

[62] ATLAS Collaboration, *Monte Carlo Calibration and Combination of In-situ Measurements of Jet Energy Scale, Jet Energy Resolution and Jet Mass in ATLAS*, ATLAS-CONF-2015-037, (2015), URL: https://cds.cern.ch/record/2044941.

[63] ATLAS Collaboration, *Performance of pile-up mitigation techniques for jets in pp collisions at* $\sqrt{s} = 8$ *TeV using the ATLAS detector*, Eur. Phys. J. C **76** (2016) 581, arXiv: 1510.03823 [hep-ex].

[64] ATLAS Collaboration, *Performance of b-jet identification in the ATLAS experiment*, JINST **11** (2016) P04008, arXiv: 1512.01094 [hep-ex].

[65] ATLAS Collaboration, *Performance of missing transverse momentum reconstruction in proton–proton collisions at $\sqrt{s}$ = 7 TeV with ATLAS*, Eur. Phys. J. C **72** (2012) 1844, arXiv: 1108.5602 [hep-ex].

[66] ATLAS Collaboration, *Estimation of non-prompt and fake lepton backgrounds in final states with top quarks produced in proton-proton collisions at $\sqrt{s}$ = 8 TeV with the ATLAS detector*, (2014), URL: http://cds.cern.ch/record/1951336.

[67] ATLAS Collaboration, *Measurement of the top quark-pair production cross section with ATLAS in pp collisions at $\sqrt{s}$ = 7 TeV*, Eur. Phys. J. C **71** (2011) 1577, arXiv: 1012.1792 [hep-ex].

[68] ATLAS Collaboration, *Measurement of the charge asymmetry in top quark pair production in pp collisions at $\sqrt{s}$ = 7 TeV using the ATLAS detector*, Eur. Phys. J. C **72** (2012) 2039, arXiv: 1203.4211 [hep-ex].

[69] ATLAS Collaboration, *A search for $t\bar{t}$ resonances using lepton-plus-jets events in proton–proton collisions at $\sqrt{s}$ = 8 TeV with the ATLAS detector*, JHEP **08** (2015) 148, arXiv: 1505.07018 [hep-ex].

[70] F. A. Berends, H. Kuijf, B. Tausk and W. T. Giele, *On the production of a W and jets at hadron colliders*, Nucl. Phys. B **357** (1991) 32.

[71] ATLAS Collaboration, *Measurements of top-quark pair differential cross-sections in the lepton+jets channel in pp collisions at $\sqrt{s}$ = 8 TeV using the ATLAS detector*, Eur. Phys. J. C **76** (2016) 538, arXiv: 1511.04716 [hep-ex].

[72] J. Erdmann et al., *A likelihood-based reconstruction algorithm for top-quark pairs and the KLFitter framework*, Nucl. Instrum. Meth. A **748** (2014) 18, arXiv: 1312.5595 [hep-ex].

[73] ATLAS Collaboration, *Measurement of the top quark mass with the template method in the $t\bar{t} \to$ lepton + jets channel using ATLAS data*, Eur. Phys. J. C **72** (2012) 2046, arXiv: 1203.5755 [hep-ex].

[74] A. Höcker et al, *TMVA - Toolkit for Multivariate Data Analysis*, (2007), arXiv: physics/0703039.

[75] R. Barlow, *SLUO Lectures on Statistics and Numerical methods in HEP, Lecure 6: Resampling and the Bootstrap*, (2000), URL: www.hep.man.ac.uk/u/roger/sluo6.ps.

[76] R. Barlow, *Systematic errors: Facts and fictions*, (2002), arXiv: hep-ex/0207026 [hep-ex].

[77] S. Frixione and B. R. Webber, *Matching NLO QCD computations and parton shower simulations*, JHEP **06** (2002) 029, arXiv: hep-ph/0204244 [hep-ph].

[78] S. Frixione, P. Nason and B. R. Webber, *Matching NLO QCD and parton showers in heavy flavor production*, JHEP **08** (2003) 007, arXiv: hep-ph/0305252 [hep-ph].

[79] B. Andersson et al., *Parton fragmentation and string dynamics*, Phys. Rept. **97** (1983) 31.

[80] B. Andersson, *The Lund model*, ISBN 9780521017343, Cambridge University Press, 1997.

[81] B. Webber, *A QCD Model for Jet Fragmentation Including Soft Gluon Interference*, Nucl. Phys. B **238** (1984) 492.

[82] ATLAS Collaboration, *Impact of fragmentation modelling on the top quark mass measurement using the ATLAS detector*, ATL-PHYS-PUB-2015-042, 2015, URL: https://cds.cern.ch/record/2054420.

[83] ATLAS Collaboration, *Measurement of $t\bar{t}$ production with a veto on additional central jet activity in pp collisions at $\sqrt{s}$ = 7 TeV using the ATLAS detector*, Eur. Phys. J. C **72** (2012) 2043, arXiv: 1203.5015 [hep-ex].

[84] ATLAS Collaboration,
Measurement of the $t\bar{t}$ production cross-section as a function of jet multiplicity and jet transverse momentum in 7 TeV proton–proton collisions with the ATLAS detector, JHEP **01** (2015) 020, arXiv: 1407.0891 [hep-ex].

[85] ATLAS Collaboration, *Comparison of Monte Carlo generator predictions to ATLAS measurements of top pair production at 7 TeV*, (2015), URL: http://cds.cern.ch/record/1981319.

[86] ATLAS Collaboration, *Comparison of Monte Carlo generator predictions for gap fraction and jet multiplicity observables in $t\bar{t}$ events*, (2014), URL: https://cds.cern.ch/record/1703034.

[87] H. L. Lai et al.,
Global QCD analysis of parton structure of the nucleon: CTEQ5 parton distributions,
Eur. Phys. J. C **12** (2000) 375, arXiv: hep-ph/9903282 [hep-ph].

[88] ATLAS Collaboration, *Determination of the jet energy scale and resolution at ATLAS using Z/γ–jet events in data at $\sqrt{s}$ = 8 TeV*, (2015), URL: http://cds.cern.ch/record/2059846.

[89] ATLAS Collaboration, *Data-driven determination of the energy scale and resolution of jets reconstructed in the ATLAS calorimeters using dijet and multijet events at $\sqrt{s}$ = 8 TeV*, (2015), URL: https://cds.cern.ch/record/2008678.

[90] ATLAS Collaboration, *Calibration of b-tagging using dileptonic top pair events in a combinatorial likelihood approach with the ATLAS experiment*, (2014), URL: http://cdsweb.cern.ch/record/1664335.

[91] ATLAS Collaboration,
Calibration of the performance of b-tagging for c and light-flavour jets in the 2012 ATLAS data,
ATLAS-CONF-2014-046, 2014, URL: https://cds.cern.ch/record/1741020.

[92] ATLAS Collaboration,
Electron and photon energy calibration with the ATLAS detector using LHC Run 1 data,
Eur. Phys. J. C **74** (2014) 3071, arXiv: 1407.5063 [hep-ex].

[93] L. Lyons et al., *How to combine correlated estimates of a single physical quantity*,
Nucl. Instr. Meth. A **270** (1988) 110.

[94] R. Nisius, *On the combination of correlated estimates of a physics observable*,
Eur. Phys. J. C **74** (2014) 3004, arXiv: 1402.4016 [physics.data-an].

[95] R. Nisius, *A ROOT class to combine a number of correlated estimates of one or more observables using the Best Linear Unbiased Estimate method*, (2015),
URL: http://blue.hepforge.org/Bluemanual.pdf.